Unstable wake dynamics of rectangular flat-backed bluff bodies with inclination and ground proximity.

Guillaume Bonnavion[1]† and Olivier Cadot[2],

[1]IMSIA, UMR 9219 ENSTA-ParisTech/CNRS/CEA/EDF, Université Paris Saclay, France
[2]School of Engineering, The University of Liverpool, Liverpool, UK

(Received xx; revised xx; accepted xx)

The paper investigates experimentally the global wake dynamics of a simplified three-dimensional ground vehicle at a Reynolds number of $Re \simeq 4.0 \times 10^5$. The after body has a blunt rectangular trailing edge leading to a massive flow separation. Both the inclination (yaw and pitch angles) and the distance to the ground (ground clearance) are accurately adjustable. Two different aspect ratios of the rectangular base are considered; wider than it is tall (minor axis perpendicular to the ground) and taller than it is wide (major axis perpendicular to the ground). Measurements of the spatial distribution of the pressure at the base and velocity fields in the wake are used as topological indicators of the flow. Sensitivity analyses of the base pressure gradient expressed in polar form (modulus and phase) varying ground clearance, yaw and pitch are performed. Above a critical ground clearance and whatever the inclination is, the modulus is always found to be large due to the permanent static symmetry-breaking instability, and slightly smaller when aligned with the minor axis of the base rather than when aligned with the major axis. The instability can be characterized with a unique wake mode, quantified by this modulus (asymmetry strength) and a phase (wake orientation) which is the key ingredient of the global wake dynamics. An additional deep rear cavity that suppresses the static instability allows a *basic flow* to be characterized. It is shown that both the inclination and the ground clearance constrain the phase dynamics of the unstable wake in such way that the component of the pressure gradient aligned with the minor axis of the rectangular base equals that of the *basic flow*. Meanwhile, the other component related to the major axis adjusts to preserve the large modulus imposed by the instability. In most cases, the dynamics explores only two possible opposite values of the component along the major axis. Their respective probability depends on the geometrical environment of the wake: base shape, body inclination, ground proximity and body supports. An expression for the lateral force coefficients taking into account the wake instability is proposed.

Key words: instability, wakes, aerodynamics

1. Introduction

The aerodynamics of ground vehicles has become a major issue in view of lowering fuel consumption and pollutant emissions. In particular, as one third of the total drag

† Email address for correspondence: guillaume.bonnavion@ensta-paristech.fr

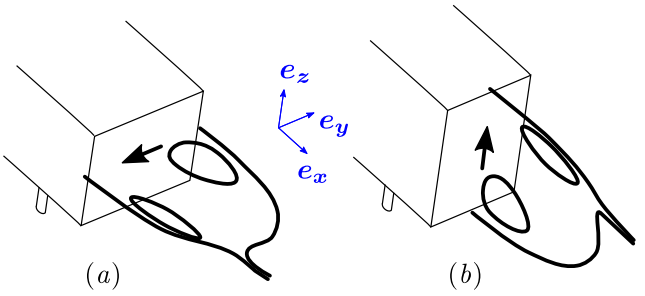

FIGURE 1. Sketches of the recirculating bubbles for the y-instability (a) and z-instability (b) interpreted from mean wake measurements of Grandemange *et al.* (2013a). Thick arrows display the corresponding base pressure gradients.

is admitted to be generated at the car's rear after body (Hucho 1998), a deeper understanding of the turbulent wake dynamics is thus of prime interest. In view of the large commercial success of minivans and sport utility vehicles, vehicle shapes with vertical after bodies are nowadays very common.

From the academic point of view, fundamental research investigates simplified geometries such as the Ahmed body (Ahmed *et al.* 1984). The square-back Ahmed body is a three-dimensional bluff body with a rectangular blunt after body producing a wide flow separation. It is known to experience a steady supercritical bifurcation in the laminar regime for a Reynolds number of $Re \simeq 340$ resulting in a permanent asymmetric state of the wake. This bifurcation was first identified experimentally by Grandemange *et al.* (2012) and recently confirmed by computation (Evstafyeva *et al.* 2017). As the Reynolds number increases, the wake undergoes random switching between two mirror asymmetric states that statistically restores symmetries. These states have been observed up to Reynolds number of 2.5×10^6 in the seminal work of Grandemange *et al.* (2013b), even with rotating wheels and road effects.

Since then, many works have reported these asymmetric states (so-called static symmetry-breaking modes) in a variety of geometries with vertical rectangular bases: flat plates (Cadot 2016), square-back Windsor model (Perry *et al.* 2016a,b; Pavia *et al.* 2018; Pavia & Passmore 2018), square-back Ahmed body both experimentally (Volpe *et al.* 2015; Brackston *et al.* 2016; Li *et al.* 2016; Barros *et al.* 2017; Evrard *et al.* 2016) and numerically (Pasquetti & Peres 2015; Evstafyeva *et al.* 2017; Lucas *et al.* 2017). Grandemange *et al.* (2013a) showed the importance of the rectangular base aspect ratio that can select either left/right or top/bottom asymmetric states of the wake, respectively called y- and z-instabilities, where y and z refer to the wake asymmetry directions as depicted in figure 1. Although the y-instability corresponds to a pure reflectionnal symmetry-breaking, the z-instability does not, strictly speaking, because of the ground and the body supports (Grandemange *et al.* 2013a).

The presence of a permanent asymmetric wake state is also a general property of turbulent wakes of axisymmetric bodies (Grandemange *et al.* 2013a, 2014a; Rigas *et al.* 2014, 2015; Gentile *et al.* 2016, 2017), reminiscent of a steady symmetry-breaking bifurcation in the laminar regime leading to an asymmetric state with planar symmetry (Pier 2008). In the turbulent regime, the azimuthal phase of the symmetry plane evolves like a random walk (Rigas *et al.* 2015) thus exploring all azimuthal angles uniformly. This infinity of directions may be interpreted as a multistable wake in opposition to rectangular bodies that just have two directions, either y or z. Therefore, three-dimensional bodies

with reflectional symmetries or with symmetry of revolution present similar stability properties.

Sensitivity analyses of the asymmetric mode to small symmetrical imperfections have been experimentally addressed, either by introducing a steady disturbance in the vicinity of the body (Vilaplana *et al.* 2013; Grandemange *et al.* 2013*a*, 2014*b*,*a*; Brackston *et al.* 2016; Barros *et al.* 2017) or by the main body inclination (Volpe *et al.* 2015; Perry *et al.* 2016*b*; Gentile *et al.* 2017). A large majority of these studies show that the imperfection selects the wake on a preferential asymmetric state, thus reducing considerably the multistable dynamics obtained without the imperfections. In the works of Barros *et al.* (2017); Gentile *et al.* (2017), this selection is modelled as a pitchfork bifurcation, with either the disturbance size or the misalignment angle as the bifurcation parameter.

These asymmetry-related instabilities have a substantial impact on the aerodynamic loading of the body as demonstrated by the fluid-structure interaction experiment of Cadot (2016). For the Ahmed body, the strategy of symmetrization of the wake either by means of passive (Grandemange *et al.* 2014*b*; Cadot *et al.* 2015; Evrard *et al.* 2016; Lucas *et al.* 2017) or active (Brackston *et al.* 2016; Li *et al.* 2016; Evstafyeva *et al.* 2017) flow control techniques leads to drag reductions up to 9%, although it is not clear yet what the real part due the instability suppression alone is.

For sake of simplicity, the wake subjected to the y- or z-instability will be called the *unstable wake* for the remainder of the paper. Variable orientations are often encountered in ground vehicle aerodynamics due to cross-winds introducing yaw, and payload mass modifying ground clearance and pitch. Most of the work done so far considered a body subjected to the y-instability aligned with the incoming flow; only few reported measurements with yaw variations (Cadot *et al.* 2015; Volpe *et al.* 2015; Perry *et al.* 2016*b*; Brackston *et al.* 2016) or ground clearance variations (Grandemange *et al.* 2013*a*; Cadot *et al.* 2015) but none with pitch variations. To the authors' knowledge, there are no results reported in the literature about the effects of yaw or pitch for a body subjected to the z-instability. There is then a fundamental issue about the unstable wake response to the body orientation. One may ask the following questions: how does the unstable wake dynamics react to small misalignment? And, what are the consequences on the aerodynamics loading of the body?

Our experimental strategy is to perform sensitivity analyses changing independently three parameters: the ground clearance c, the yaw β and the pitch α with and without the instability by repeating the analyses with a deep rear cavity known as an efficient way to suppress the asymmetric states of the wake (Evrard *et al.* 2016; Lucas *et al.* 2017). The study is extended for a second after body designed to develop the z-instability. As introduced by Grandemange *et al.* (2013*b*), we use the spatial distribution of the pressure at the body base as a topological indicator of the turbulent wake state. Rigas *et al.* (2014, 2015) successfully applied the same technique to an axisymmetric body with a blunt trailing edge and proposed an insightful low-dimensional physical model of the axisymmetric turbulent wake dynamics.

The paper is organized as follows. The experimental setup is described in § 2. Results in § 3 are split into two parts, §§ 3.1 and 3.2 respectively investigating the y-instability and z-instability. For the y-instability, sensitivity analyses of the base pressure gradient varying ground clearance, yaw and pitch are presented in § 3.1.1 and then repeated in § 3.1.2 with an additional rear deep cavity to suppress the instability. In the third part § 3.1.3, the lateral aerodynamic force is examined in the light of the base pressure gradient contribution with and without the instability. A relationship summarizing the measurements linking lateral force coefficients and the base pressure gradient is given. For the z-instability, sensitivity analyses of the base pressure gradient varying clearance,

yaw and pitch are presented in § 3.2.1 and then yaw sensitivities are repeated in § 3.2.2 for different ground clearances to evidence the two branches of most probable states of the wake. In the third part § 3.2.3, the vertical aerodynamic force is examined in the light of the base pressure gradient contribution. Results lead to two discussions, the role of the phase dynamics for a three-dimensional turbulent wake in § 4.1 and the wake instability adaptation mechanism with the body orientation in § 4.2. Finally, § 5 concludes and offers perspectives on the paper.

2. Experimental setup

2.1. *Apparatus*

The three-dimensional bluff bodies considered in this work are two flat-backed Ahmed bodies (Ahmed *et al.* 1984) drawn in figure 2. They are composed of the same main body supported by four vertical cylinders and with two interchangeable after bodies. The characteristic dimensions are given in table 1. The aspect ratio of the rectangular base is $W/H = 1.174$ for the square-back after body (model used in Evrard *et al.* (2016)) and $w_b/H = 0.940$ for the boat-tailed after body. The first geometry is known to be subjected to the y-instability (Evrard *et al.* 2016) while the second geometry has been designed to develop the z-instability by reducing the base aspect ratio, accordingly to Grandemange *et al.* (2013*a*). The boat-tail shape is a circle arc tangential to the main body, characterized by two parameters, the boat-tail length ℓ_B and the angle θ_B (see figure 2*d* and table 1). The rear of the square-back after body is equipped with a sliding board of dimensions $(H - 20\ \text{mm}) \times (W - 20\ \text{mm})$ displayed as the dashed rectangle in figure 2(*d*). A cavity of depth d is then produced by pushing the board towards the interior of the body as in Evrard *et al.* (2016). For the present study, the cavity depth remains fixed to $d/H = 0.285$ which has been shown by the experiments of Evrard *et al.* (2016) and the computation of Lucas *et al.* (2017) to suppress the y-instability.

The height of the body H and the main incoming velocity U_∞ are chosen respectively as length and velocity scaling units. For the remainder of the paper any quantity a with superscript a^* is expressed in these non-dimensional units. For instance, the non-dimensional time is defined as $t^* = (tU_\infty)/H$, the aspect ratio of the rectangular base $W^* = W/H$. The coordinate system used throughout is defined in figure 2 with its origin set at the centre of the base of the models.

The ground clearance c^* (normal distance from the body to the ground) can be adjusted at the front within the range $c_f^* \in [0.050, 0.170]$ and independently at the rear, c_r^* within an identical range. These displacements are controlled by two Standa 8MVT188-20 translation stages placed inside the body and driven by a 8SMC4-USB controller. The repeatability and the precision of the ground clearance is, in non-dimensional value, $\delta c^* \simeq 3.4 \times 10^{-3}$. The independence of each axis allows for a pitch angle given by $\tan\alpha = (c_f - c_r)/\Lambda_{fr}$, where Λ_{fr} is the wheelbase, kept constant owing to a sliding system mounted inside the body. The angle is counted positively in the clockwise orientation as shown in figure 2(*a*) and is varied in the range $\alpha \in [-1.5°, 1.5°]$. The yaw angle β, defined in figure 2(*b*), can be adjusted by means of a rotating table mounted in the test section floor. This angle is counted following the direct orientation, the value $\beta = 0°$ corresponding to the body aligned with the incoming flow. It is considered aligned when, for a baseline ground clearance of $c^* = 0.168$, the left and right orientations of the wake subjected to the y-instability are equally explored for the duration of observation. The actual angle of the square-back body with respect to the wind tunnel is $\beta_w = -0.4°$,

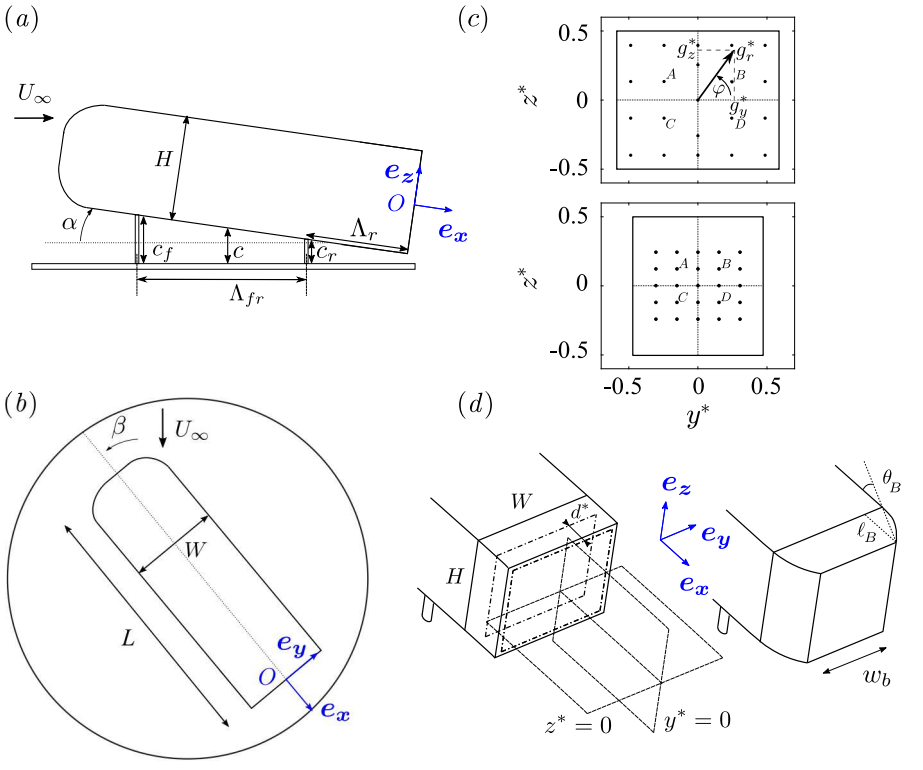

FIGURE 2. Experimental apparatus: schematic side view (a), top view (b) of the main body and rear views (c) of the square-back (top) and boat-tailed (bottom) body bases. In (c), the bases of the models are equipped with pressure sensors (black dots); the four points A, B, C, D are used for calculation of the base pressure gradient $\hat{\boldsymbol{g}}^*$ (see text). Schematic view (d) of the square-back (left) and boat-tailed (right) after bodies and representation of the fixed horizontal and vertical laser planes used for Particle Image Velocimetry. They correspond to $y^* = 0$ and $z^* = 0$ for the aligned body case. The rectangular board that creates the cavity of the square-back after body (when pushed inwards the body) is shown by the dashed rectangles in (d) for $d^* = 0$ and $d^* = 0.285$.

where β_w is the angle between the wind tunnel longitudinal axis and the body. The yaw angle is varied in the range $\beta \in [-6.0°, 6.0°]$.

The experiments are carried out at the GIE-S2A in Montigny-le-Bretonneux (France) in a closed-loop model-scale wind tunnel dedicated to automotive aerodynamics. The incoming flow is a 3/4 open-jet with a cross-section of 2.60 m $\times$ 1.47 m. The plenum dimensions are 9.30 m $\times$ 6.60 m $\times$ 4.15 m and the contraction ratio is 1 : 6. The thickness of the boundary layer is controlled by suction so that its displacement thickness equals $\delta_1^* = 1.0 \times 10^{-2}$ at a distance $l_0^* = 4.70$ upstream of the nose of the model. The flow inhomogeneity is lower than 0.5% with an angular deviation smaller than 0.25° at the considered regime. The free-stream velocity is set to $U_\infty = 20.0$ m.s^{-1} and the temperature inside the vein is regulated at $T_\infty = 293.15$ K with an uncertainty of less than 0.1 m.s^{-1} and 0.5 K respectively. Under those conditions, the corresponding Reynolds number is $Re = U_\infty H/\nu \simeq 4.0 \times 10^5$, ν being the air kinematic viscosity.

2.2. *Pressure measurements*

Unsteady pressure is measured at the $N = 21$ locations (y_i^*, z_i^*) indicated by the black dots at the base of the body in figure 2(c). The sampling frequency is set at 200 Hz

Dimension	Dimensional value	Dimensionless value based on H
Height of the body H:	0.298 m	1.000
Width of the body W:	0.350 m	1.174
Length of the body L:	0.994 m	3.336
Wheelbase Λ_{fr}:	0.477 m	1.601
Track:	0.290 m	0.973
Supports diameter:	0.020 m	0.067
Location of rear supports Λ_r:	0.290 m	0.973
Projected surface area S:	0.104 m^2	1.174
Width of the base w_b:	0.350 m / 0.280 m	1.174 / 0.940
Length of the boat tail ℓ_B:	0.160 m	0.537
Angle of the boat tail θ_B:	12.5°	

TABLE 1. Dimensions of the Ahmed body for the two after body geometries.

per channel with an accuracy of ±3.75 Pa and measurements are performed thanks to a Scanivalve ZOC22b pressure scanner connected to a Green Lake Engineering Smart-ZOC100 electronics. The low-pass cut-off frequency due to the tubing lengths between the pressure holes on the body and the pressure scanner is approximately 50 Hz which is enough for the time resolution requested for the present study. The free-stream static pressure p_∞, obtained directly from the facility, is used to compute the instantaneous pressure coefficient:

$$c_p(y^*, z^*, t^*) = \frac{p(y^*, z^*, t^*) - p_\infty}{\frac{1}{2}\,\rho\,U_\infty^2} \tag{2.1}$$

where ρ denotes the air density. The uncertainty on the pressure coefficient is approximately 2×10^{-3}.

The instantaneous base suction coefficient $c_b(t^*)$ is computed from the average on the $N = 21$ pressure taps at the base:

$$c_b(t^*) = -\frac{1}{N}\sum_{i=1}^{N} c_p(y_i^*, z_i^*, t^*) \tag{2.2}$$

This coefficient is always positive in separated flow areas and follows similar trends as the total drag of the model (Roshko 1993).

Following the same experimental procedure as Grandemange *et al.* (2013*a*), four pressure sensors are used to compute the base pressure gradient which is representative of the instantaneous configuration of the wake. First, a horizontal component g_y^* is computed as follows using the sensors marked A, B, C and D in figure 2(*c*):

$$g_y^*(t^*) = \frac{1}{2} \times \left[\frac{c_p(y_A^*, z_A^*, t^*) - c_p(y_B^*, z_B^*, t^*)}{y_A^* - y_B^*} + \frac{c_p(y_C^*, z_C^*, t^*) - c_p(y_D^*, z_D^*, t^*)}{y_C^* - y_D^*} \right] \tag{2.3}$$

where y_i^* and z_i^* stand for the coordinates of sensor i. The same process is repeated to compute the vertical component g_z^* using the pairs (A, C) and (B, D). Finally, the complex base pressure gradient is obtained as $\hat{g}^* = g_y^* + \mathrm{i}\, g_z^*$ where $\mathrm{i}^2 = -1$. The modulus $g_r^* = |\hat{g}^*|$ and the argument $\varphi = \arg(\hat{g}^*)$ of the polar form will be referred to as strength and phase of the base pressure gradient.

2.3. *Aerodynamic load measurements*

A six-component aerodynamics balance provided by Schencker GmbH and located beneath the wind tunnel floor is used to obtain time series of the aerodynamic forces at

a sampling frequency set at 10 Hz. The model is connected to the balance by the four cylindrical supports. The forces (F_x, F_y, F_z) are the components of the total aerodynamic load $\boldsymbol{F}$ in the coordinate system described above. The uncertainty is 0.3 N for the drag F_x and the side force F_y, whilst it is approximately 0.5 N for the lift F_z. The model frontal surface S is used to compute the force coefficients:

$$c_i = \frac{F_i}{\frac{1}{2}\,\rho\,U_\infty^2\,S}, \quad i = x, y, z \tag{2.4}$$

with a corresponding maximum uncertainty of 10^{-3}.

2.4. *Velocity measurements*

Velocity fields are measured using two-dimensional Particle Image Velocimetry (PIV) equipment. It is based on a dual pulse Nd:YAG laser (200 mJ, 4 ns) creating a laser sheet whose thickness is 5 mm and combined with a Dantec FlowSense EO 4 MPx CCD camera. Image pairs are shot at a rate of 4 Hz and 400 snapshots are recorded. The interrogation window size is set to 32×32 pixels, which corresponds to a physical size $\Delta_y^* \times \Delta_z^* = 0.017 \times 0.017$ (or $\Delta_x^* \times \Delta_z^* = 0.017 \times 0.017$ for vertical planes) and with an overlap of 50%. We investigate the two orthogonal planes fixed in the laboratory frame and located at the base of the body: a vertical one at mid-width that will be referred to as the $y^* = 0$ plane and a horizontal one that will be referred to as the $z^* = 0$ plane. Both planes are shown in figure 2(d). Actually, when either a pitch or a yaw angle is introduced, the local coordinate system $(\boldsymbol{e}_x, \boldsymbol{e}_y, \boldsymbol{e}_z)$ associated with the base in figure 2(d) will not coincide with the PIV measurements fields anymore. Since the considered angles are small (less than 2°), it was decided for the sake of simplicity to keep the same name for the space coordinates of the velocity fields. Using conventional notations, the PIV gives access to the field $\boldsymbol{u}_{xz}^* = u^*\boldsymbol{e}_x + w^*\boldsymbol{e}_z$ in the $y^* = 0$ plane and to $\boldsymbol{u}_{xy}^* = u^*\boldsymbol{e}_x + v^*\boldsymbol{e}_y$ in the $z^* = 0$ plane.

2.5. *Experimental protocol*

Before each set of experiments, acquisitions of both the pressure and the forces are performed in no-wind conditions for a duration of 10 s. The no-wind data are then averaged and subtracted from the force balance and pressure measurements. Regular tares are performed and zero values are checked to ensure accuracy, repeatability and reliability of the results.

Simultaneous base pressure and aerodynamic load measurements are recorded during $t = 180$ s (*i.e.* $t^* = 12080$ in dimensionless units). Although this is not long enough to achieve complete statistical convergence (which in fact is a challenge to fulfill because of the long-time dynamics), this duration was chosen as a compromise that is sufficient to identify the most probable values.

Since the paper focuses on the long-time dynamics of the unstable wake, base pressure and force balance data are low-pass filtered at $f_c = 2$ Hz (*i.e.* $f_c^* = 0.03$) by means of a moving average using a 0.5 s time window. As the natural cut-off frequency of the two measurements systems is larger, both sets of filtered data are comparable with an accurate frequency resolution.

In addition to those measurements, PIV is performed in the two planes described in § 2.4. Base pressure measurements are made during the acquisition in order to perform conditional averaging based on synchronous measurements. For PIV measurements, snapshots are acquired during $t = 100$ s (*i.e.* $t^* = 6711$ in dimensionless units).

	w_b^*	C_b	C_b'	C_x	C_x'	C_y	C_y'	C_z	C_z'
$d^*=0$	1.174	0.183	0.006	0.287	0.004	−0.003	0.020	−0.118	0.005
$d^*=0.285$	1.174	0.137	0.006	0.259	0.004	−0.003	0.005	−0.122	0.004
$d^*=0$	0.940	0.124	0.002	0.279	0.002	−0.001	0.003	−0.158	0.002

TABLE 2. Characteristic mean and fluctuating coefficients for baseline configurations defined as $c^*=0.168, \alpha=0^\circ, \beta=0^\circ$ without ($d^*=0$) and with ($d^*=0.285$) the rear cavity for the square-back geometry ($w_b^*=1.174$) and for the boat-tailed geometry ($w_b^*=0.940$).

3. Results

We recall that the superscript * indicates a quantity made non-dimensional using the uniform incoming flow velocity U_∞ and the body height H. Lower case letters x are used for an instantaneous variable while upper case letters $X=\overline{x}$ denote the temporal averaging of the variable. The Reynolds notation is also used for fluctuations, $x(t)=X+x'(t)$ for which the standard fluctuation is $X'=\sqrt{\overline{x'^2}}$.

For the remainder of the paper, we will call the baseline the case where $\beta=\alpha=0^\circ$ with a ground clearance $c^*=0.168$. It is a similar configuration to that of Ahmed *et al.* (1984). We show in table 2 characteristic properties of the baseline without ($d^*=0$) and with the rear cavity ($d^*=0.285$). The drag coefficient of the baseline without the cavity lies within the range $0.25\leqslant C_x\leqslant 0.35$ reported in the literature (Ahmed *et al.* 1984; Barros *et al.* 2014; Volpe *et al.* 2015; Evrard *et al.* 2016). For the square-back geometry, the large magnitude of the side force fluctuation $C_y'=0.020$ (compared to those of the other components in table 2) reveals the y-instability through the bi-stable dynamics (Grandemange *et al.* 2013*b*; Evrard *et al.* 2016). The rear cavity produces a drag reduction of 9.7% together with strong attenuation of the side force fluctuation in conformity with Evrard *et al.* (2016); Lucas *et al.* (2017).

The first part of the results in § 3.1 will consider the square-back geometry with the aim of performing sensitivity analyses of the y-instability. While the presence of a y-instability is easily detectable because of the reflectionnal symmetry breaking in the y-direction, it is much more difficult to diagnose the z-instability. Actually there is no reflectionnal symmetry to break in the z-direction because of the ground proximity and body supports. There is also no obvious reason to observe bistability that would unambiguously reveal the presence of the z-instability. The second part of the results in § 3.2 will consider the boat-tailed geometry in order to investigate sensitivity analyses of the z-instability.

3.1. *The y-instability*

This section presents results about the square-back geometry only. In § 3.1.1, we show sensitivity maps of the base pressure gradient responses to variations of the ground clearance c^*, the yaw angle β and the pitch angle α around the baseline. The responses are assessed through the statistics of the base pressure gradient $\hat{g}^*$ considering each component of both coordinate systems $(g_y^*,\ g_z^*)$ and $(g_r^*,\ \varphi)$ by representing its probability density function f normalized by its most probable value. The resulting plots are four two-dimensional sensitivity maps for each of the three geometrical configurations varying the geometrical parameter $q=c^*,\alpha$ or β: $f(q,g_y^*)$, $f(q,g_z^*)$, $f(q,g_r^*)$ and $f(q,\varphi)$. The wake dynamics and topology are then investigated for chosen specific configurations reflecting all situations. In § 3.1.2, the procedure is repeated with the rear cavity. In

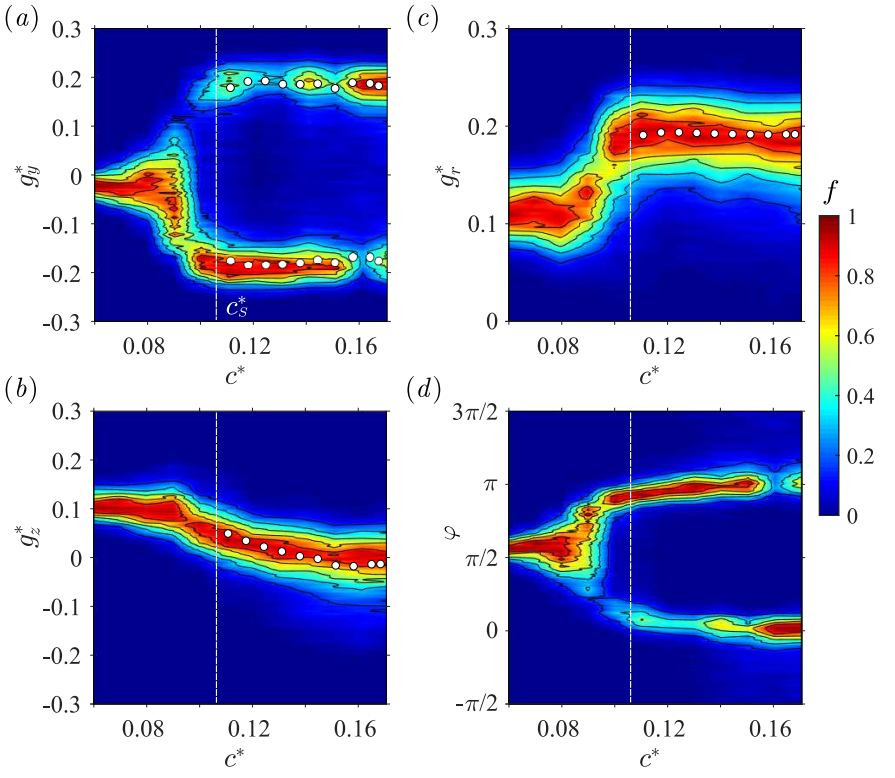

FIGURE 3. Base pressure gradient response to a variation of the ground clearance c^* for the square-back body. Sensitivity maps (*a*) $f(c^*, g_y^*)$, (*b*) $f(c^*, g_z^*)$, (*c*) $f(c^*, g_r^*)$ and (*d*) $f(c^*, \varphi)$. The clearance $c_S^* \simeq 0.105$ is defined as the threshold from which the instability is saturated. See discussion § 4.1 for white symbols.

§ 3.1.3, the aerodynamic force sensitivity is examined and compared to the base pressure gradient contribution with and without the rear cavity.

3.1.1. *Wake sensitivity to the body clearance and inclinations*

The four sensitivity maps of the base pressure gradient due to the variation of the ground clearance c^* are shown in figure 3(*a*,*b*) for the Cartesian components and figure 3(*c*,*d*) for the polar form. When the body is gradually raised in figure 3(*a*), the most probable branch for g_y^* observed for $c^* < 0.080$ bifurcates in two symmetrical branches resulting from an instability. This was already fully described by Grandemange *et al.* (2013*a*); Cadot *et al.* (2015) showing that the ground proximity suppresses the instability towards a symmetric wake through a pitchfork bifurcation. The region we consider is for large values of c^* for which the wake dynamics is dominated by the stochastic exploration of the two symmetric branches. Independently of the sign of g_y^* (*i.e.* the random switching dynamics) the permanent asymmetry introduced by the symmetry-breaking (SB) modes can be seen in the modulus g_r^* displayed in figure 3(*c*). The modulus saturates to a constant value when $c^* > c_S^* \simeq 0.105$ as shown in the figures. The regime $c^* > c_S^*$ corresponds to the unstable wake due to the y- or z-instability (Grandemange *et al.* 2013*a*), and will be referred to as the saturated regime throughout. The interesting result is that, whilst the vertical base pressure gradient g_z^* decreases significantly, the gradient modulus g_r^* remains constant and corresponds to a change in the gradient orientation φ.

For the next two series of experiments concerning yaw and pitch sensitivities, we will

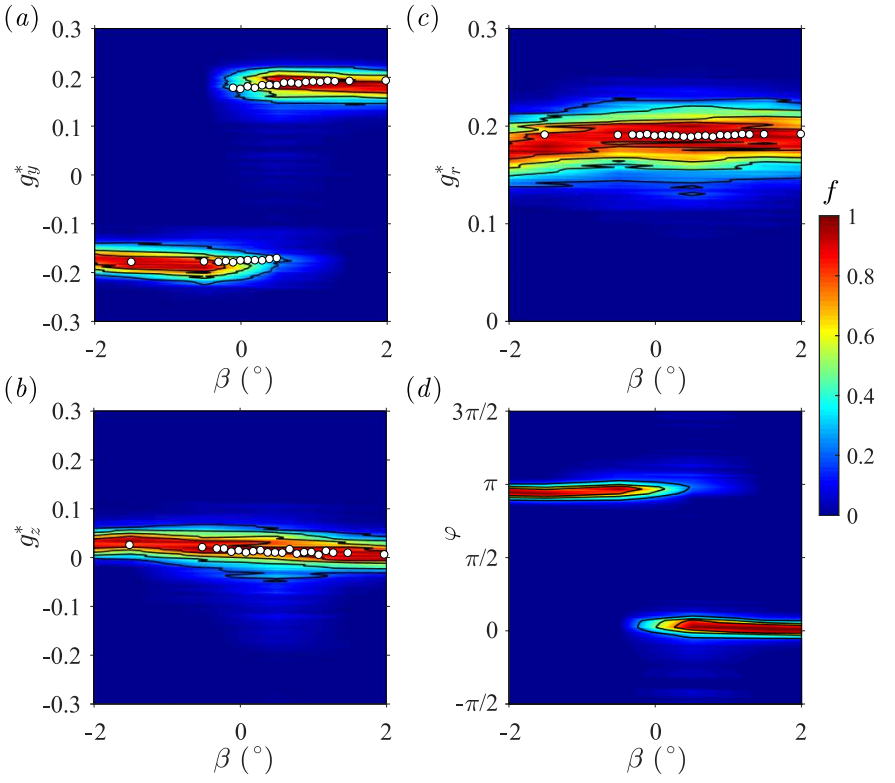

FIGURE 4. Base pressure gradient response to variations of the yaw angle β for the square-back body. Sensitivity maps (*a*) $f(\beta, g_y^*)$, (*b*) $f(\beta, g_z^*)$, (*c*) $f(\beta, g_r^*)$ and (*d*) $f(\beta, \varphi)$. See discussion § 4.1 for white symbols.

consider small variations of the inclination around the baseline (see table 2). The baseline has most probable gradients that take phase values very close to $\varphi \simeq 0$ or π and a modulus $g_r^* \simeq 0.187$ obtained in figure 3(*c*).

The sensitivity analysis to small variations of the yaw angle β with a fixed ground clearance $c^* = 0.168$ and pitch $\alpha = 0°$ is shown in figure 4. The main result observed in figure 4(*a*) and previously reported in Volpe *et al.* (2015); Cadot *et al.* (2015); Evrard *et al.* (2016) is a discontinuous transition between two opposite branches of g_y^* which implies a phase jump (figure 4*d*) between values close to 0 and π. Nevertheless, this transition occurs with a fairly constant modulus g_r^* as shown in figure 4(*c*). The vertical component g_z^* in figure 4(*b*) has a slight unexpected affine variation with the yaw which is likely to be due to an imperfection of the set-up, coming from multiple sources such as wind inhomogeneity, non-zero roll angle and cable passage behind the rear right-hand side cylindrical support. Because of the constant modulus, the setup imperfections affect slightly the phase φ (figure 3*d*) which slightly deviates from $\varphi_0 = 0$ or $\varphi_0 = \pi$.

We now turn to the sensitivity to the pitch angle α. The yaw angle is set to $\beta = 0°$ and the front and rear ground clearances are adjusted for a given pitch but keeping $c^* = \frac{1}{2}(c_f^* + c_r^*) = 0.168$ in order to recover the baseline when $c_f^* = c_r^*$. The sensitivity results of the base pressure gradient are shown in figure 5. Looking at figure 5(*a*), which shows the sensitivity of the horizontal gradient component g_y^*, we can distinguish three regimes. At large nose-down, for $\alpha \lesssim -0.75°$, there is a single branch located around $g_y^* = 0$, which bifurcates in two opposite branches in the range $-0.75° \lesssim \alpha \lesssim 0.5°$. In

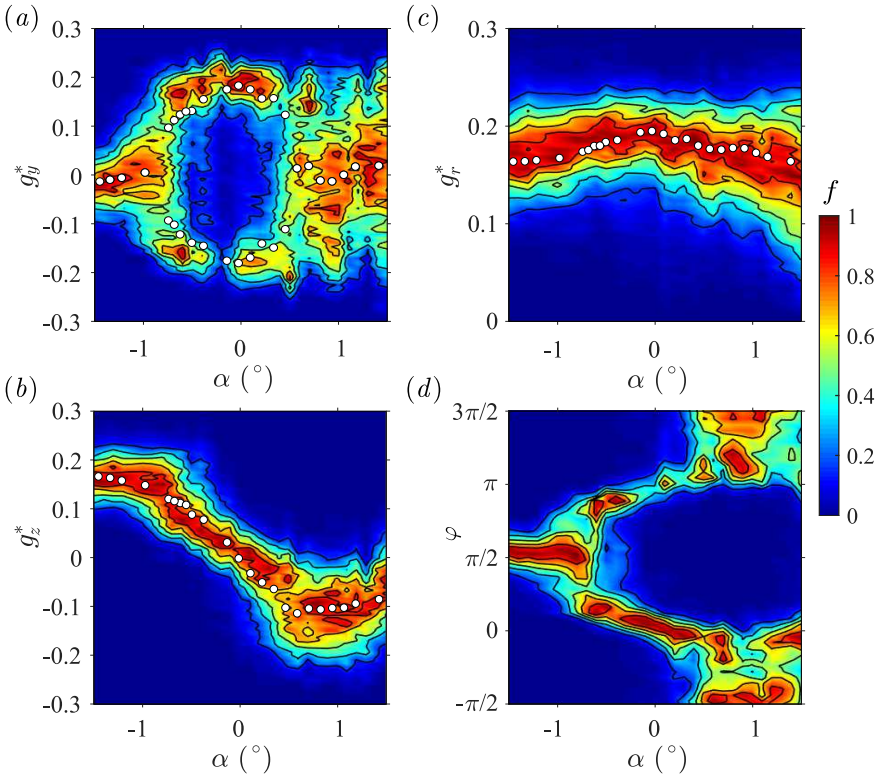

FIGURE 5. Base pressure gradient response to variations of the pitch angle α for the square-back body. Sensitivity maps (*a*) $f(\alpha, g_y^*)$, (*b*) $f(\alpha, g_z^*)$, (*c*) $f(\alpha, g_r^*)$ and (*d*) $f(\alpha, \varphi)$. See discussion § 4.1 for white symbols.

the last regime with nose-up, for which $\alpha \gtrsim 0.5°$, the horizontal component varies almost uniformly in a wide range $|g_y^*| \lesssim 0.2$.

The effect of the pitch on the vertical gradient component g_z^* is shown in figure 5(*b*). It displays a monotonic variation with the pitch angle in the range $-0.75° \lesssim \alpha \lesssim 0.5°$ coincidently with the two branches observed for g_y^*. Apart from this range, the vertical component is saturated to extreme values. Although these three regimes are very different, the modulus shown in figure 5(*c*) displays an almost symmetric evolution, with decreases on both sides of the maximum. In the third regime, the phase is unlocked in the $[-\pi, 0]$ interval with a rather uniform exploration (figure 5*d*), unlike nose-down regimes. This different behavior is attributed to the wall proximity at the trailing edge which has a major effect on the base flow in nose-up configurations.

Most importantly, a similar conclusion as for the ground clearance and the yaw experiments can be drawn. The small pitch angle variation produces a component g_z^* of the vertical pressure gradient. The modulus g_r^* is slightly modulated, maximum for horizontal orientation and minimum for vertical one.

The wake dynamics of the four configurations of the base pressure gradient orientations: vertical positive, horizontal (positive and negative) and vertical negative is now respectively investigated through the pitch angles $\alpha = -1°$, $\alpha = 0°$ and $\alpha = 1°$. We show the corresponding time series of the gradient modulus $g_{r\alpha}^*(t^*)$ and phase $\varphi_\alpha(t^*)$ in figure 6. The nose-down at $\alpha = -1°$ in figure 6(*a*) clearly depicts a phase lock-in for $\varphi_{-1°}(t^*)$ at $\pi/2$ with turbulent fluctuations. When the pitch is set to zero (baseline configuration),

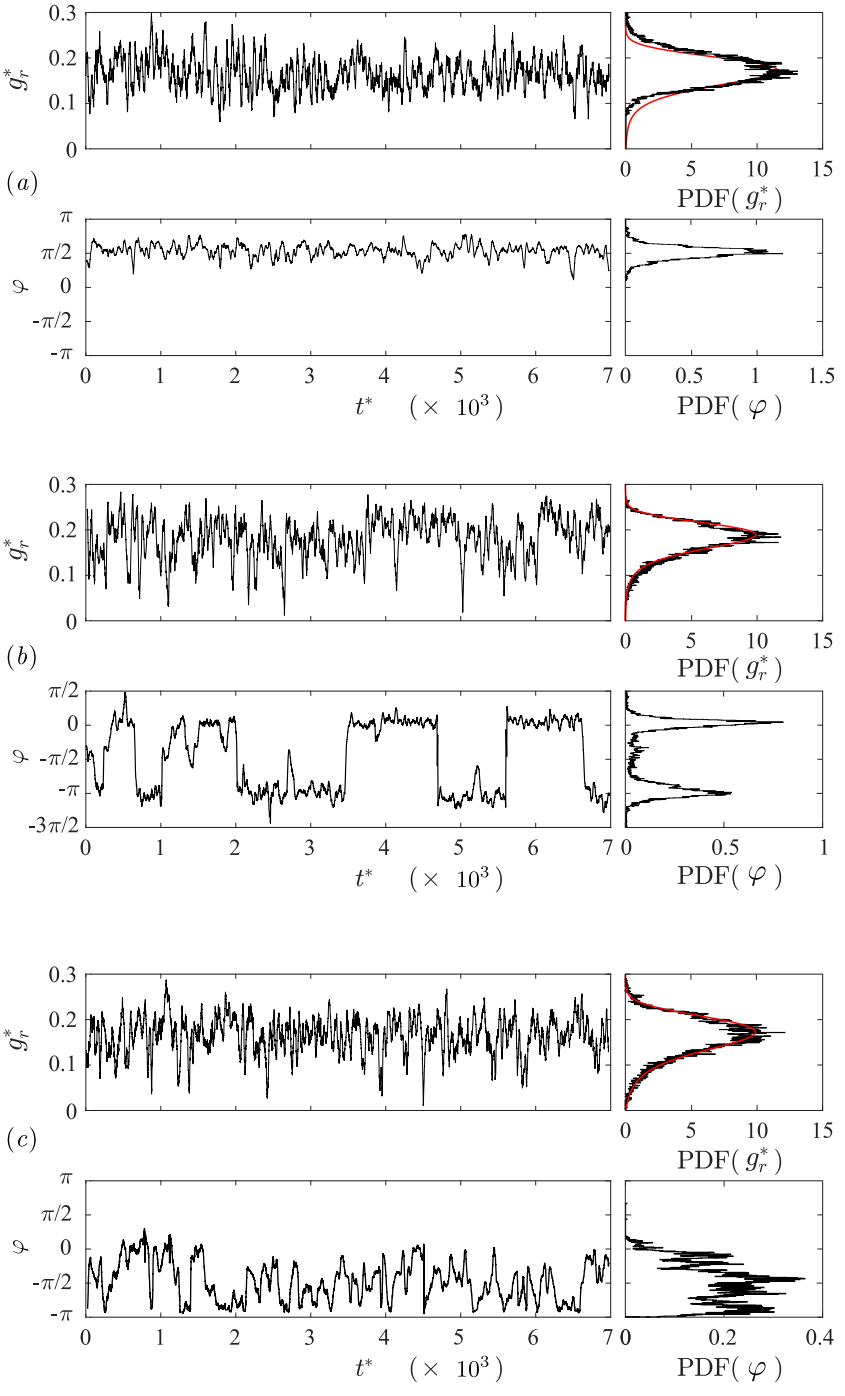

FIGURE 6. Modulus $g^*_{r\alpha}(t^*)$ and phase $\varphi_\alpha(t^*)$ time series (left) of the base pressure gradient for the square-back body. Corresponding probability density functions (right) for (a) nose-down $\alpha = -1^\circ$, (b) baseline $\alpha = 0^\circ$ and (c) nose-up $\alpha = +1^\circ$. The smooth red lines superimposed to PDF(g_r^*) in (a), (b) and (c) are best fits of Rigas *et al.* (2015)'s PDF model; the three parameters of the fit are not given.

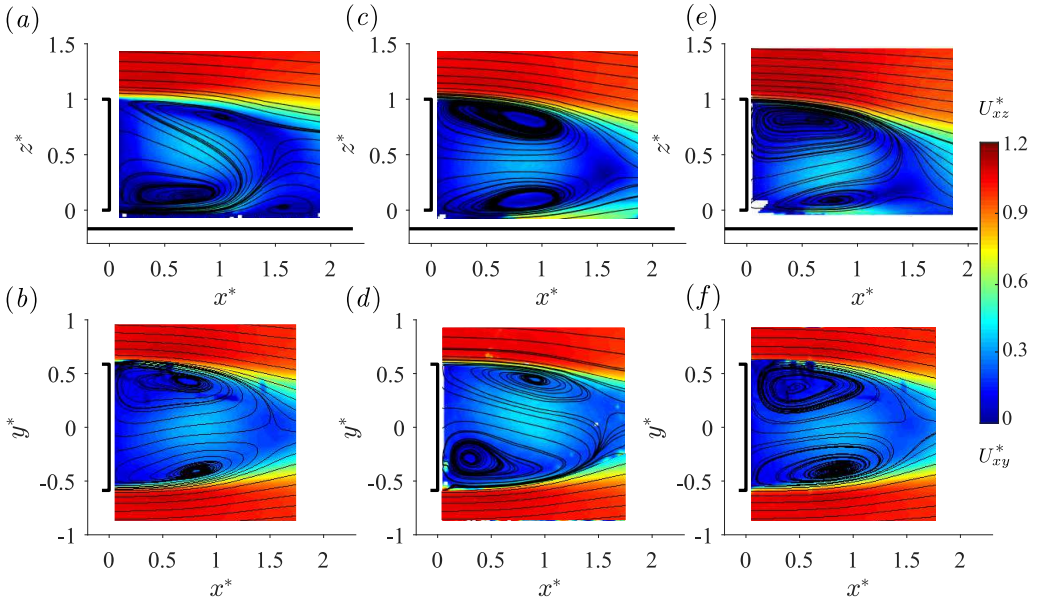

FIGURE 7. Cross-sections of the mean velocity field of the square-back body visualized using streamlines superimposed to the modulus of the components in the vertical plane (x^*, z^*) (top row) and horizontal plane (x^*, y^*) (bottom row) for (a, b) nose-down $\alpha = -1°$, (c, d) baseline $\alpha = 0°$ (P state, see text) and (e, f) nose-up $\alpha = +1°$.

the phase dynamics in figure 6(b) consists of random jumps of π and elsewhere to very long-time duration of typically $\delta t^* = 1000$ of phase lock-in at 0 and $-\pi$. This long-time bi-stable dynamics was fully described in Grandemange *et al.* (2013*b*) using Cartesian coordinates for the gradient. It is worth mentioning that the dynamics is not only mainly made of phase jumps, since some events of the phase $\varphi_{0°}$ occur around $-\pi/2$ with long-time evolution related to phase drift or wake rotation (see for instance within the time interval $[1; 2] \times 10^3$ in figure 6b). For the nose-up case, there is no phase lock-in but large phase fluctuations associated with random wake rotations exploring the range $[-\pi, 0]$ with some phase jumps like the one observed at $t^* = 4.5 \times 10^3$ in figure 6(c). There are obviously some similarities with the diffusive dynamics of the turbulent axisymmetric wake of Rigas *et al.* (2014, 2015), the main difference being the random walk of the phase that is bounded. Since the modulus is decoupled from the phase in Rigas *et al.* (2015)'s model, it is possible to present a best fit of the statistics of the gradient modulus g_r^* shown as the red lines in figure 6.

In the following, N and P states terminology refer to negative and positive horizontal base pressure gradient as introduced by Grandemange *et al.* (2013*b*). Making use of this definition, the state depicted in figure 1(a) is state N. The mean flows of the wake measured in the two perpendicular planes confirm the four different wake orientations according to the base pressure gradient alignments. For the baseline case, the mean flow has been conditioned by $-\frac{\pi}{2} < \varphi_{0°} < \frac{\pi}{2}$ in order to capture the P state only (*i.e.* phase lock-in $\varphi_{0°}(t*) \simeq 0$) in figures 7($c, d$). The N state (*i.e.* phase lock-in $\varphi_{0°}(t*) \simeq \pi$) is not shown. It is the mirror of the P state using the transformation $(y^*, z^*) \to (-y^*, z^*)$. We can see in figure 7 that the strong wake asymmetry is successively detected in the $y^* = 0$ plane in figure 7(a), in the $z^* = 0$ plane in figure 7(d) and in the $y^* = 0$ plane in figure 7(e) while the wake in the other perpendicular plane is always more symmetric. They respectively correspond to the phase lock-in $\varphi_{-1°} \simeq \pi/2$ (figure 7a, b),

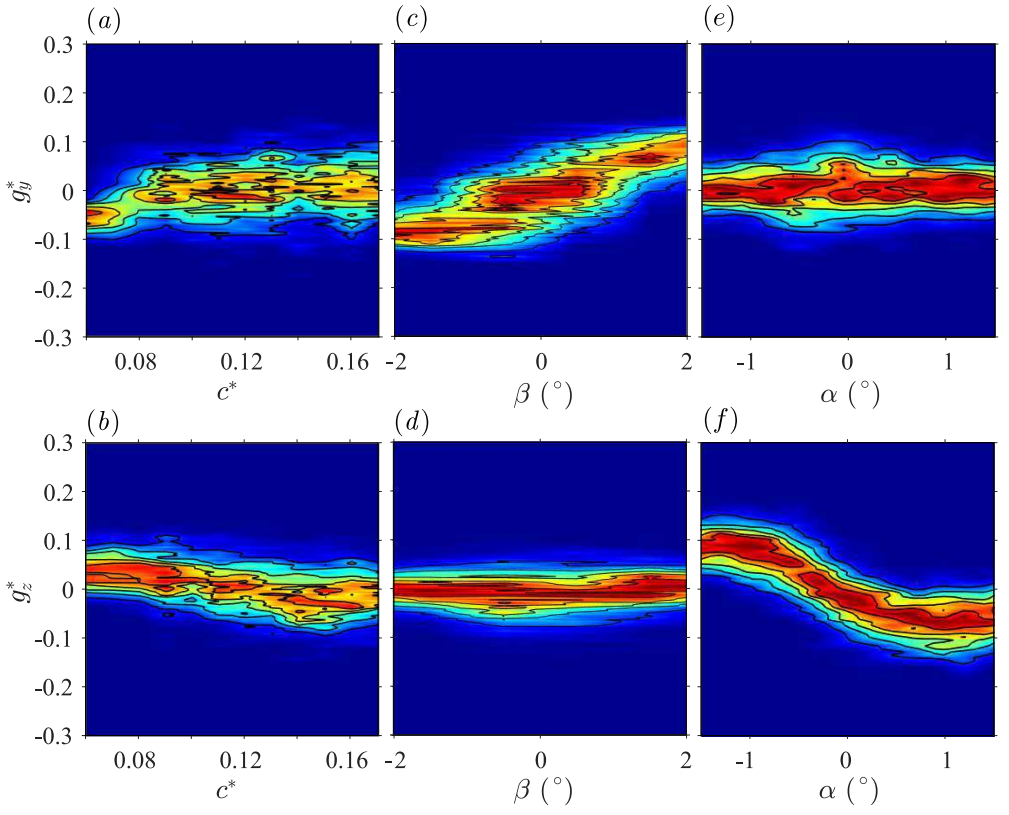

FIGURE 8. Base pressure gradient response to ground clearance c^* (a, b), yaw β (c, d) and pitch angle α (e, f) variations for the square-back body with a rear cavity. Sensitivity maps f (same color bar for f as in figures 3, 4, 5) of the horizontal component g_y^* (a, c, e) and vertical component g_z^* (b, d, f).

$\varphi_{0^\circ} \simeq 0$ (state P in figure 7c, d) or equivalently $\varphi_{0^\circ} \simeq \pi$ (state N, not shown) and finally to the mean orientation (with $-\pi < \varphi_{1^\circ}(t^*) < 0$) towards a negative vertical pressure gradient (figure 7e, f). A **supplementary movie** provides the dynamics of wake pressure imprints at the base of the body for the pitch angles from which pressure gradients shown in figure 6 are extracted.

As a summary of the wake sensitivity to the body orientation in the saturated regime of the instability, it is found that independently of the phase dynamics, the modulus of the base pressure gradient depends upon the vector orientation, maximum for a horizontal alignment with $g_r^*(0 \text{ or } \pi) \simeq 0.187$ and minimum for a vertical alignment with $g_r^*(\frac{\pi}{2}) \simeq 0.159$. Ground clearance, yaw and pitch variations produce a vertical component g_z^* of the pressure gradient that constrains the phase dynamics because of the modulus properties. Different phase dynamics scenarios have been identified: phase locks-in, phase jumps and bounded drifts. As depicted in the mean PIV fields, the phase of the base pressure gradient is confirmed to be an accurate indicator of the global wake orientation.

3.1.2. *Wake sensitivity with a rear cavity*

The sensitivity analyses have been repeated in exactly the same conditions but with the rear cavity. For the sake of brevity, the three sensitivity experiments are grouped in figure 8 for Cartesian coordinates and in figure 9 for the polar form. The ground clearance bifurcation observed in figure 3(a) has been completely suppressed by the rear

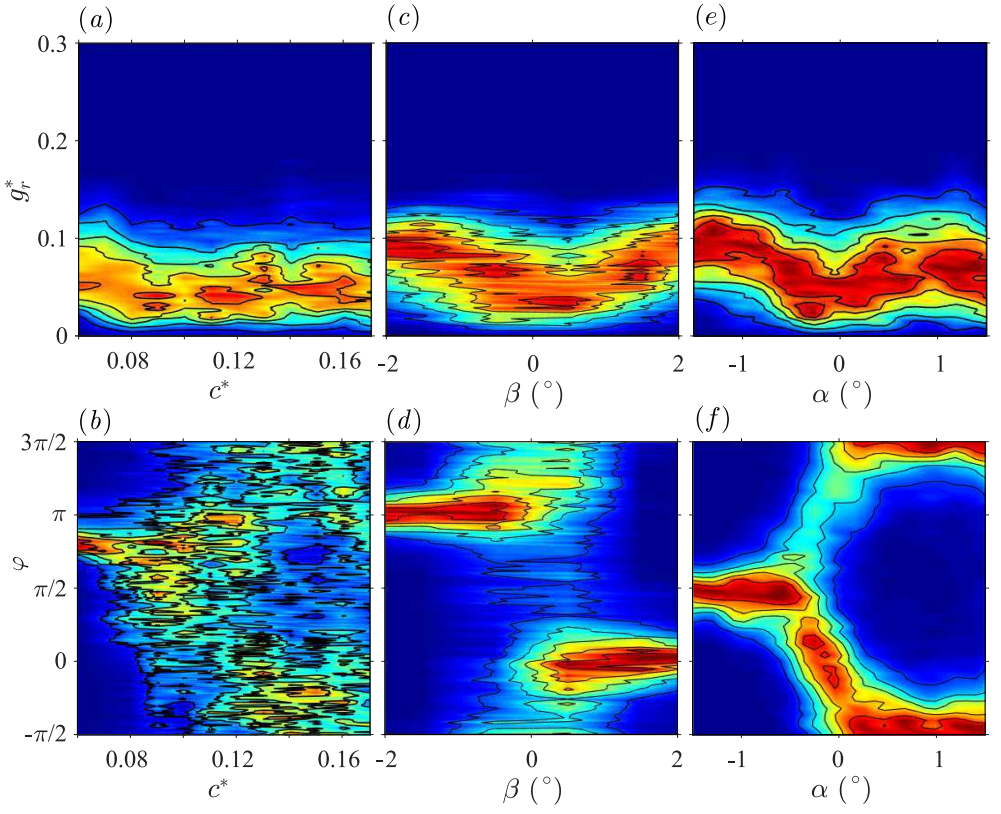

FIGURE 9. Base pressure gradient response to ground clearance c^* (a, b), yaw β (c, d) and pitch angle α (e, f) variations for the square-back body with a rear cavity. Sensitivity maps f (same color bar for f as in figures 3, 4, 5) of the gradient modulus g_r^* (a, c, e) and phase φ (b, d, f).

cavity in figure 8(a) as expected because of the stabilization observed by Evrard *et al.* (2016). For the baseline configuration with the rear cavity, both Cartesian components of the base gradient are approximately zero. From figures 8(c, d, e, f), we see that a slight change of yaw (respectively the pitch) shifts almost linearly the horizontal component g_y^* (respectively vertical component g_z^*) while the other component g_z^* (respectively g_y^*) remains constant. However, even with the cavity, a saturation of the varying component is observed for angles, either yaw or pitch, larger than $\pm 1°$ in figure 8(c) and (f).

The modulus and phase sensitivity maps are shown in figure 9. Despite the fact that the modulus is considerably reduced (by more than a factor 2), it is now a function of the yaw and pitch angles that reaches a minimal value around the baseline where the gradient changes sign. The complex phase dynamics observed without the cavity (phase drifts and jumps) is now replaced by trivial permanent lock-in except when the phase is poorly defined for small modulus. This loss of phase dynamics is the consequence of the suppression of the wake instability.

The mean wake of the body with the rear cavity is presented in figure 10 which can be directly compared to the same plane views without the cavity in figure 7. The wake observed for the nose-down configuration at $\alpha = -1°$ in figure 10(a, b) is similar to that of the figure 7(a, b) albeit that with the cavity the separation from the ground is prevented in figure 10(a) and the wake reflectional symmetry is better checked in figure 10(b). For the baseline configuration in figure 10(c, d) the wake is fully symmetrized as in Evrard

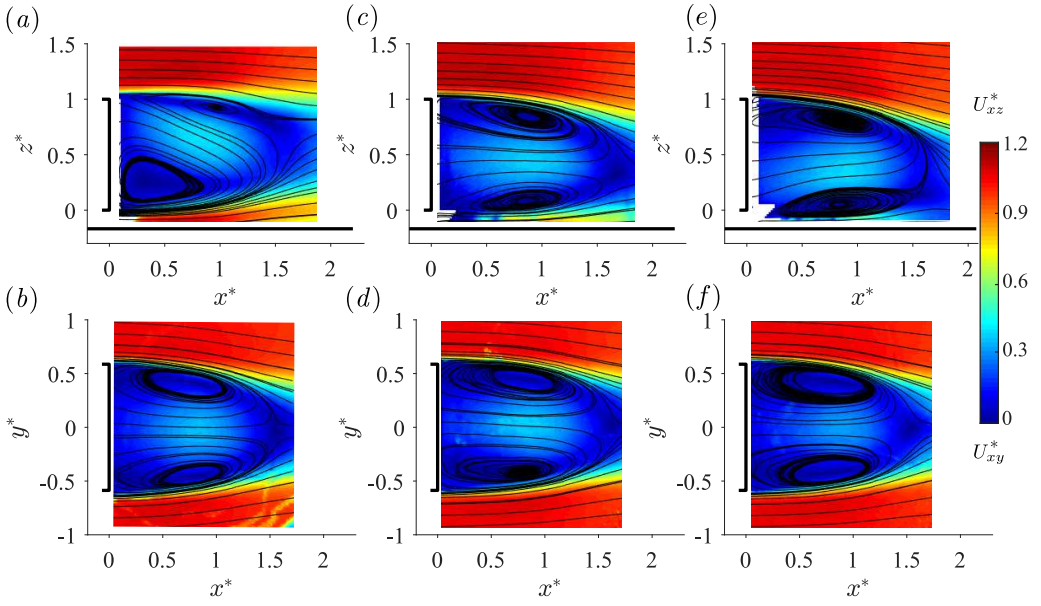

FIGURE 10. Cross-sections of the mean velocity field of the square-back body with the rear cavity visualized using streamlines superimposed to the modulus of the components in the vertical plane (x^*, z^*) (top row) and horizontal plane (x^*, y^*) (bottom row) for (a, b) nose-down $\alpha = -1°$, (c, d) baseline $\alpha = 0°$ and (e, f) nose-up $\alpha = +1°$.

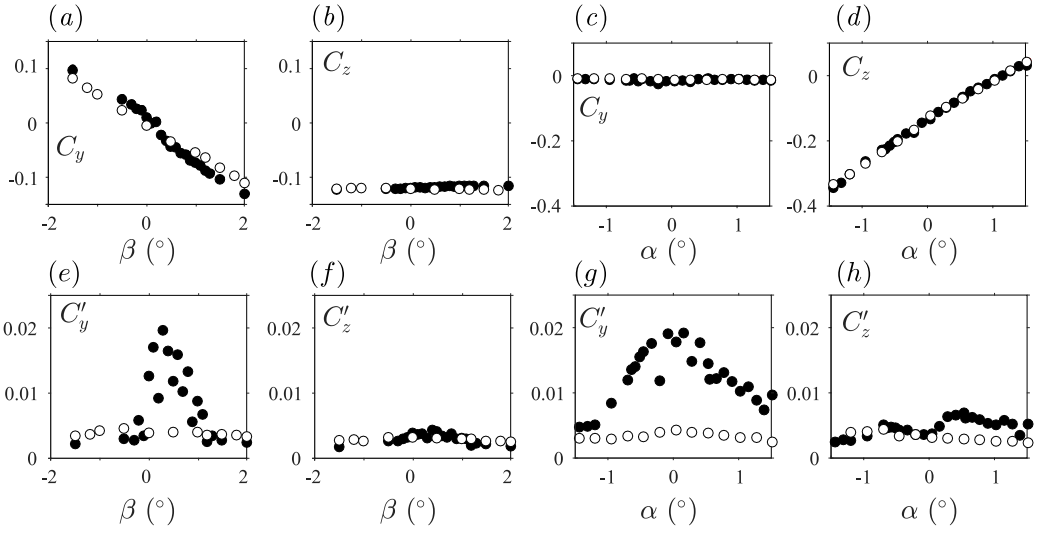

FIGURE 11. Mean (top row) and fluctuating (bottom row) cross-flow force coefficients vs. yaw (a, b, e, f) and pitch angle (c, d, g, h) of the square-back body (black filled circles) and with the rear cavity (empty circles).

et al. (2016); Lucas *et al.* (2017). The wake for the nose-up configuration at $\alpha = +1°$ in figure 10(e, f) is also quite similar to that of figure 7(e, f) without the cavity. Hence, for the two extreme cases $\alpha = \pm 1°$, the pitch angle of the body orientates the wake in the vertical direction with a similar strength as without the cavity.

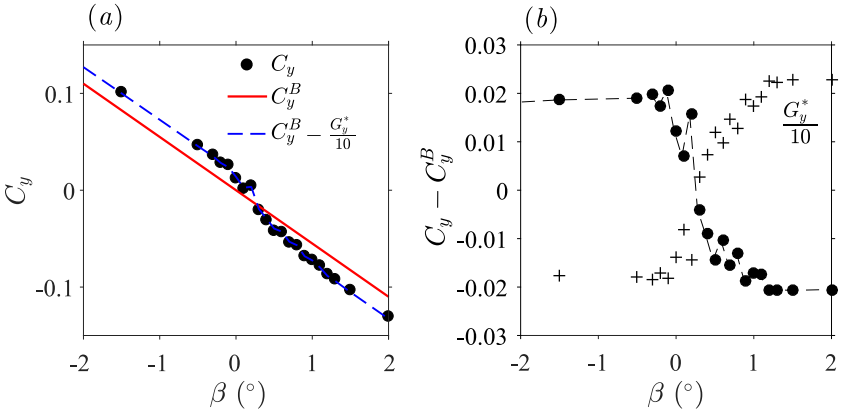

FIGURE 12. Mean side force coefficient vs. yaw β of the square-back body. In (a), measured force coefficient (symbols), basic flow coefficient (red line) and coefficient computed from equation (3.1) (blue dashed line, see text). In (b), mean contribution of the instability $C_y - C_y^B$ (filled circles) and mean horizontal base pressure gradient G_y^* (crosses).

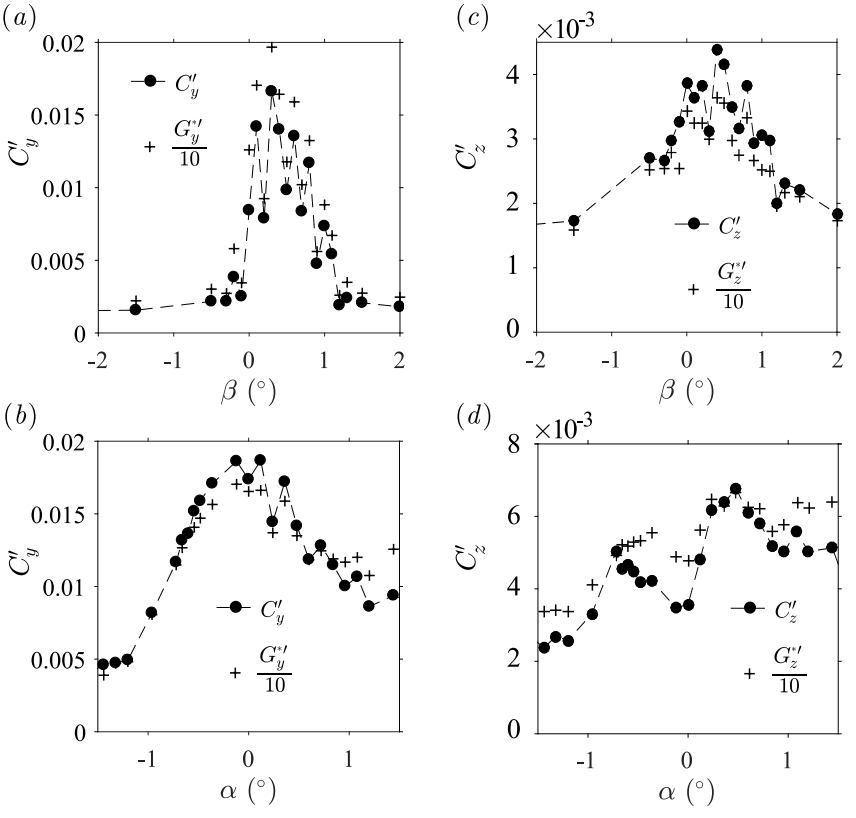

FIGURE 13. Components of the fluctuation force coefficients of the square-back body C_y' and C_z' (filled circles) compared to the fluctuation base pressure gradient $G_y^{*\prime}$ and $G_z^{*\prime}$ (crosses) vs. yaw β (top row) and pitch angle α (bottom row).

3.1.3. *Global force sensitivity versus wake aerodynamic loading*

The y- and z-components of the mean force coefficients obtained for the yaw and pitch sensitivity experiments are shown in figure $11(a-d)$ with and without the rear cavity. A clear stabilization of the unstable wake can be seen in the mean horizontal y-component in figure $11(a)$ obtained with the yaw variations. The nonlinear behavior due to the instability (also reported in Perry *et al.* (2016*b*)) is replaced by a linear law with the cavity. For the other mean coefficients, we can hardly distinguish any effect induced by the rear cavity. For the force coefficient fluctuations shown in figure $11(e-h)$, one can observe fluctuation crisis each time phase unlocking occurs.

Figure $11(a)$ suggests that the mean side force coefficient C_y^B obtained without the instability (the superscript ^{B} will refer to this *basic flow*) should evolve linearly with β as for the cavity experiment. The force coefficient $C_y^B(\beta) = -0.055 \times \beta$ (where β is expressed in degrees), simply obtained from a linear fit of the cavity experiment, is shown in figure $12(a)$ as the red straight line. We compare the strength of the instability $C_y - C_y^B$ to the mean horizontal base pressure gradient G_y^* in figure $12(b)$. The two curves are satisfactorily proportional such that the mean side force coefficient can be directly related to the mean base gradient as:

$$C_y = C_y^B - \frac{G_y^*}{10} \tag{3.1}$$

We can see in figure $12(a)$ the good agreement of (3.1) (blue dashed line) with the experimental data (symbols). An instantaneous relationship can be speculated from (3.1) to take into account the unsteady loading due to the wake instability through the dynamics of the base gradient:

$$c_y(t^*) = C_y^B - \frac{g_y^*(t^*)}{10} \tag{3.2}$$

implying that $C_y' = G_y^{*\prime}/10$. The fluctuation force coefficient C_y' is plotted in figure $13(a)$ for yaw variation and figure $13(b)$ for pitch variation and matches satisfactorily with ${G^*}'_y/10$.

Since the mean lift coefficient C_z is not affected by the instability (no differences in figure $11(b)$ and (d) with or without the rear cavity), we can state that for the vertical force coefficient:

$$C_z = C_z^B \tag{3.3}$$

regardless of the base pressure gradient orientation. Again, an instantaneous relationship but with only the fluctuations of the vertical gradient component can be speculated:

$$c_z(t^*) = C_z^B - \frac{{g^*}'_z(t^*)}{10} \tag{3.4}$$

implying that ${C_z}' = G_z^{*\prime}/10$. Although the fluctuations are much smaller vertically than horizontally, we still see good agreements of (3.4) in figures $13(c)$ and (d).

One may wonder if a similar relationship could be obtained from the drag c_x and the base suction c_b coefficients. Actually, independently of the ground clearance, the yaw or the pitch, the rear cavity has a beneficial effect on the mean base suction or mean drag coefficient that are respectively reduced within the ranges $[23\%, 25\%]$ and $[9.5\%, 10.5\%]$ as can be seen in figure $14(a$-$d)$. Comparable drag reduction is also observed below the instability threshold ($c^* < 0.105$). As shown in Lucas *et al.* (2017), a deep rear cavity has a primary effect of considerably lengthening the recirculating region towards the inside of the body. Consequently, low pressure sources therein are reduced independently

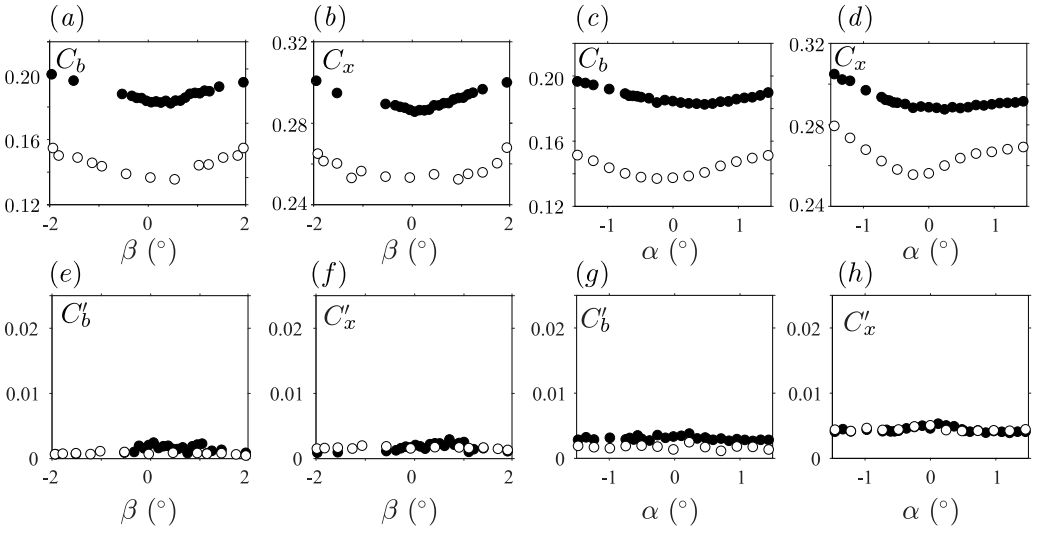

FIGURE 14. Mean (top row) and fluctuating (bottom row) drag force and base suction coefficients vs. yaw (a, b, e, f) and pitch angle (c, d, g, h) of the square-back body (black filled circles) and with the rear cavity (empty circles).

from the symmetry properties of the wake. It then remains impossible to distinguish the contribution from the wake symmetrization due to the instability suppression to this strong mean flow modification. Hence, from our point of view, the drag of the basic flow C_x^B is not extractable from the data. Considering all yaw and pitch variations, the fluctuations of both the base suction and drag remain almost identical to those of the baseline given in table 2 as can be seen in figure 14(*e-h*). There are then no consequences of the unstable wake phase dynamics on these coefficients. The reason is that base suction is more related to the magnitude of the gradient's modulus that was shown to be almost constant rather than to its orientation. The correlation between base suction and the gradient's modulus was previously reported in the sensitivity analysis to a disturbance placed in the wake by Grandemange *et al.* (2014*b*) or instantaneously by Evrard *et al.* (2016).

3.2. *The z-instability*

This section presents the results about the boat-tailed geometry depicted in figure 2(*d*) and with a base aspect ratio of $w_b^* = 0.940$. In § 3.2.1, we show sensitivity maps of the base pressure gradient responses to variations of the ground clearance c^*, the yaw angle β and the pitch angle α around the baseline exactly as in § 3.1.1. The wake topologies and dynamics are then investigated for chosen specific configurations reflecting all situations. The yaw sensitivities are repeated in § 3.2.2 for different ground clearances to evidence the two branches of most probable states of the wake. The aerodynamic force is examined in a third part § 3.2.3.

3.2.1. *Wake sensitivity to the body clearance and orientations*

The four sensitivity maps of the base pressure gradient due to the variation of the ground clearance c^* are shown in figure 15(*a*,*b*) for the Cartesian components and figure 15(*c*,*d*) for the polar form. When the ground clearance is gradually increased in figure 15(*a*), the horizontal component g_y^* remains almost around zero. The vertical component g_z^* (figure 15*b*) experiences a jump for $c^* \simeq 0.080$ from a positive branch

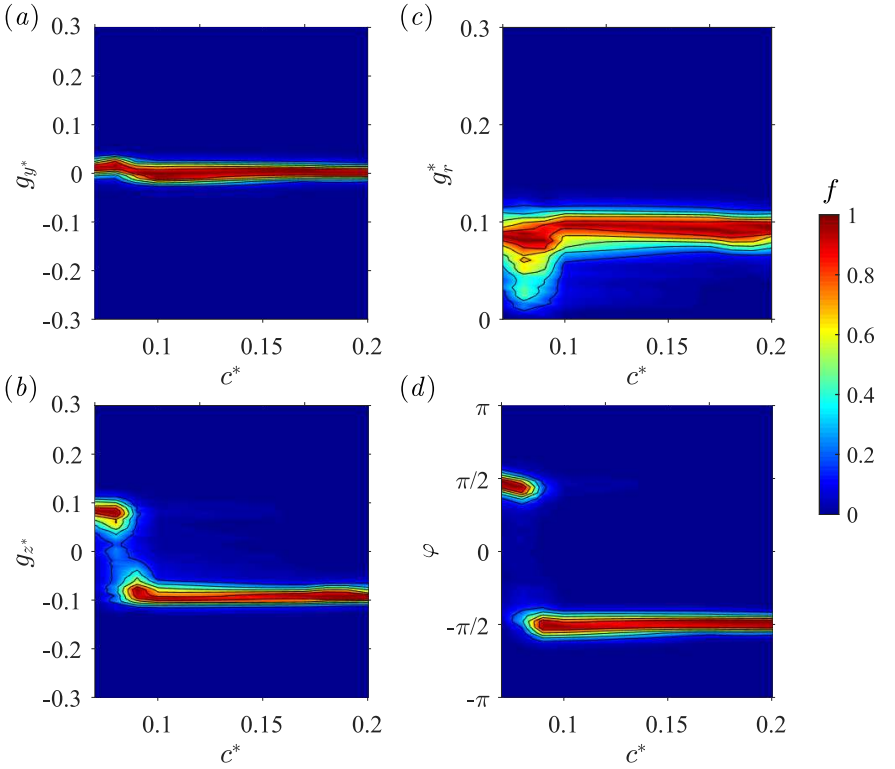

FIGURE 15. Base pressure gradient response to a variation of the ground clearance c^* for the boat-tailed body. Sensitivity maps (*a*) $f(c^*, g_y^*)$, (*b*) $f(c^*, g_z^*)$, (*c*) $f(c^*, g_r^*)$ and (*d*) $f(c^*, \varphi)$.

($g_z^* \simeq 0.1$) to a negative one ($g_z^* \simeq -0.1$). A bistable dynamic is then obtained around $c^* \simeq 0.080$. In the experiment of Grandemange *et al.* (2013*a*), the ground clearance is non-dimensionalized using the body width, $c_W^* = c^*/W^*$, and the z-instability is found to saturate on the positive branch only for a ground clearance $c_{SW}^* \simeq 0.060$ and then switches to the negative branch at $c_W^* \simeq 0.1$. Our experiment satisfactorily reproduces the switch from the positive to the negative branch but with smaller ground clearance. Using non-dimensionalisation of Grandemange *et al.* (2013*a*), the switch we observe at $c^* \simeq 0.080$ in figure 15 is within the range $0.068 \lesssim c_W^* \lesssim 0.085$ when translated using either W^* or w_b^* of the boat-tailed body. The range remains below the value $c_W^* \simeq 0.1$ of Grandemange *et al.* (2013*a*). This can be ascribed to a Reynolds number effect, which is approximately ten times larger in the present study ($Re \simeq 4.0 \times 10^5$) than in Grandemange *et al.* (2013*a*) ($Re \simeq 4.5 \times 10^4$). It is in accordance with Reynolds number effect studied in Cadot *et al.* (2015) who report 30% decrease of the critical ground clearance for the y-instability when the Reynolds number is increased from 1.7×10^4 to 1.6×10^5. The critical ground clearance c_S^* of the z-instability is not observed in our study because it is below the minimal value $c^* = 0.05$ allowed by the set-up. It is also found that the critical ground clearance is larger for the y-instability than for the z-instability as in Grandemange *et al.* (2013*a*). The modulus g_r^* displayed in figure 15(*c*) has a value close to 0.1 that is smaller than the modulus found within the range $0.15 - 0.2$ (see figures 3*c*, 4*c*, 5*c*) in § 3.1 for the square-back body. This must be ascribed to the different after body geometry. The larger fluctuations observed for $c^* \simeq 0.080$ are a consequence of the bi-stable dynamics at the branches switch in figure 15(*d*).

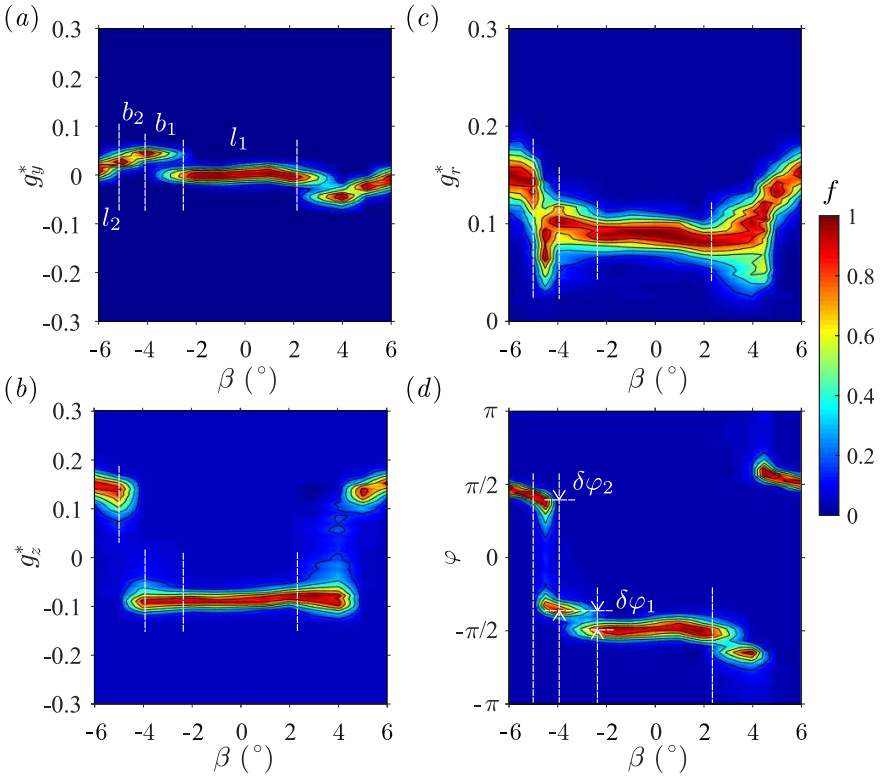

FIGURE 16. Base pressure gradient response to variations of the yaw angle β for the boat-tailed body. Sensitivity maps (*a*) $f(\beta, g_y^*)$, (*b*) $f(\beta, g_z^*)$, (*c*) $f(\beta, g_r^*)$ and (*d*) $f(\beta, \varphi)$.

For the next two series of experiments concerning yaw and pitch sensitivities, we will consider small variations of the inclination around the baseline with characteristics given in table 2.

The sensitivity analysis to the yaw angle β with a fixed pitch $\alpha = 0°$ is shown in figure 16. The results being reasonably symmetric with respect to β, we only comment the part for $\beta < 0°$. From these figures, four distinctive regions can be observed, successively named l_1, b_1, b_2 and l_2 in figure 16(*a*). They are delimited in all the figures by vertical dashed lines. In region l_1 the base pressure gradient remains almost identical to that of the baseline: it is locked with a vertical direction orientated towards the ground corresponding to $\varphi \simeq -\pi/2$ in figure 16(*d*) and a modulus close to $g_r^* \simeq 0.1$ in figure 16(*c*). When the yaw angle β is increased, the wake becomes bi-stable in the region b_1 and the gradient experiences small phase jumps of amplitude $\delta\varphi_1 \simeq \pi/7$ without noticeable changes in the modulus g_r^*. This small lateral bistability has not been observed for yaw experiments at lower ground clearance – for which transitions occur at smaller angles – presented in § 3.2.2. Although not discernible on the side pressure measurements, it is suspected to be caused by premises of separation on the leeward boat-tail. For larger yaw angles, another bi-stable regime in b_2 is observed with much larger phase jumps of $\delta\varphi_2 \simeq 3\pi/4$ in figure 16(*d*) associated with large fluctuations of the modulus. In the last regime l_2, the gradient is locked with a vertical direction orientated towards the top ($\varphi \simeq +\pi/2$) and a modulus close to $g_r^* \simeq 0.15$. The main result is that the yaw around $\beta = \pm 4.5°$ triggers the switch of the negative vertical pressure gradient component of the baseline observed in l_1 to a positive vertical component in l_2 as clearly shown in figure 16(*b*).

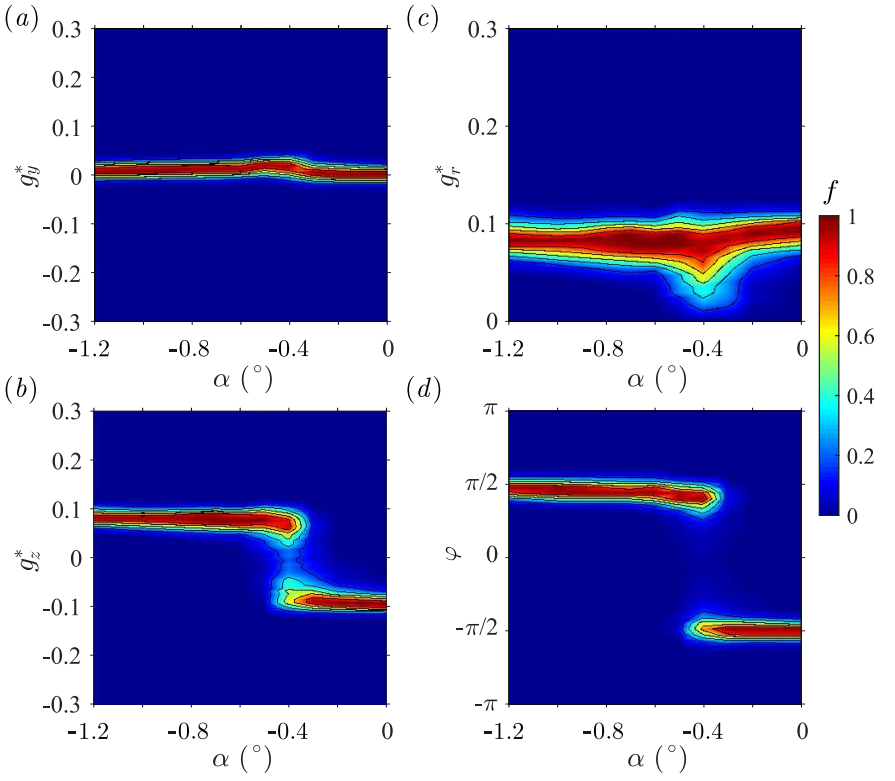

FIGURE 17. Base pressure gradient response to variations of the pitch angle α for the boat-tailed body. Sensitivity maps (*a*) $f(\alpha, g_y^*)$, (*b*) $f(\alpha, g_z^*)$, (*c*) $f(\alpha, g_r^*)$ and (*d*) $f(\alpha, \varphi)$.

The sensitivity towards the pitch angle α is now given in figure 17. For this experiment, the yaw angle is set to $\beta = 0°$ and, as in § 3.1, the front and rear ground clearances are adjusted for a given pitch but keeping $c^* = \frac{1}{2}(c_f^* + c_r^*) = 0.168$. Based on the mechanism identified for the y-instability in § 3.1, we restricted the range of pitch angles to nose-down configurations for which a clear transition is observed. The pitch angle has almost no effect on the horizontal component in figure 17(*a*) except for a disturbance around $\alpha = -0.4°$ that corresponds to the switching region with a bi-stable dynamic in figure 17(*b*) of the vertical component of the gradient.

The successive experiments changing ground clearance, pitch and yaw mainly show that for the boat-tailed body subjected to the z-instability, two principal orientations of the base pressure gradient are observed: almost positive vertical and negative vertical. The phase then remains locked except for the bi-stable dynamics where the wake switches between opposite orientations. The dynamics of the two bi-stable cases b_1 and b_2 evidenced during the yaw sensitivity in figure 16(*c*) is respectively presented in figure 18(*a*) and figure 18(*b*). The bi-stable dynamics b_2 is similar to that obtained in ground clearance sensitivity (figure 15*c*) and pitch sensitivity (figure 17*c*) analyses. The striking observation is that the rate of random switching between the two most probable phases is substantially larger than that of the bi-stable wake subjected to the y-instability in figure 6(*b*). For the most important bi-stable behaviour that involves vertical wake reversals in figure 18(*b*), approximately 50 switches are observed against only 9 in figure 6(*b*) for horizontal wake reversals. This trend was checked for all bi-

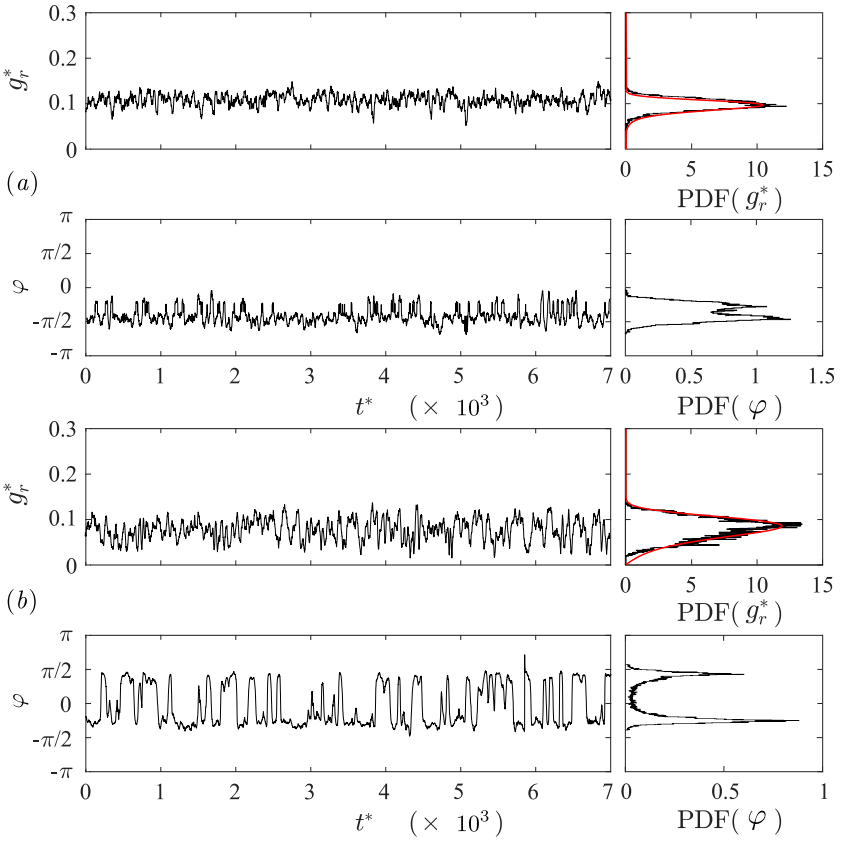

FIGURE 18. Modulus $g^*_{r\alpha}(t^*)$ and phase $\varphi_\alpha(t^*)$ time series (left) of the base pressure gradient for the boat-tailed body. Corresponding probability density functions (right) for (a) $\beta = -3°$, (b) $\beta = -5°$. The smooth red lines superimposed to PDF(g_r^*) in (a) and (b) are best fits of Rigas *et al.* (2015)'s PDF model; the three parameters of the fit are not given.

stable cases, thus confirming that the characteristic time of the random switching is approximately five times smaller for the z-instability than for the y-instability.

The different wake configurations are illustrated by their mean flow in the vertical plane in figure 19 together with their corresponding mean base pressure distribution. Because of the boat tailing, the after body develops four strong longitudinal vortices at each corner of the base affecting considerably the mean bubble closure in the figures 19 compared to that observed for the square-back after body in figures 7 and 10. For the baseline in figure 19(a), the negative vertical pressure gradient observed in the pressure distribution is associated with a skewed feedback flow orientated towards the bottom edge of the base that is the best topological indicator of the z-instability. We have identified wake reversals from the baseline for each of the three sensitivity experiments either by decreasing the ground clearance, increasing the yaw angle or by pitching down the body. For a lower ground clearance, the wake has effectively switched to the opposite base pressure gradient in figure 19(b) with a skewed feedback flow orientated to the top edge of the base. For a large yaw in figure 19(c), the switch from the baseline is not clearly observable in the vertical velocity field, while it is clearly established in the corresponding pressure distribution. Finally, for large nose-down pitch, the skewed feedback flow and the pressure distribution are clearly inverted from those of the baseline.

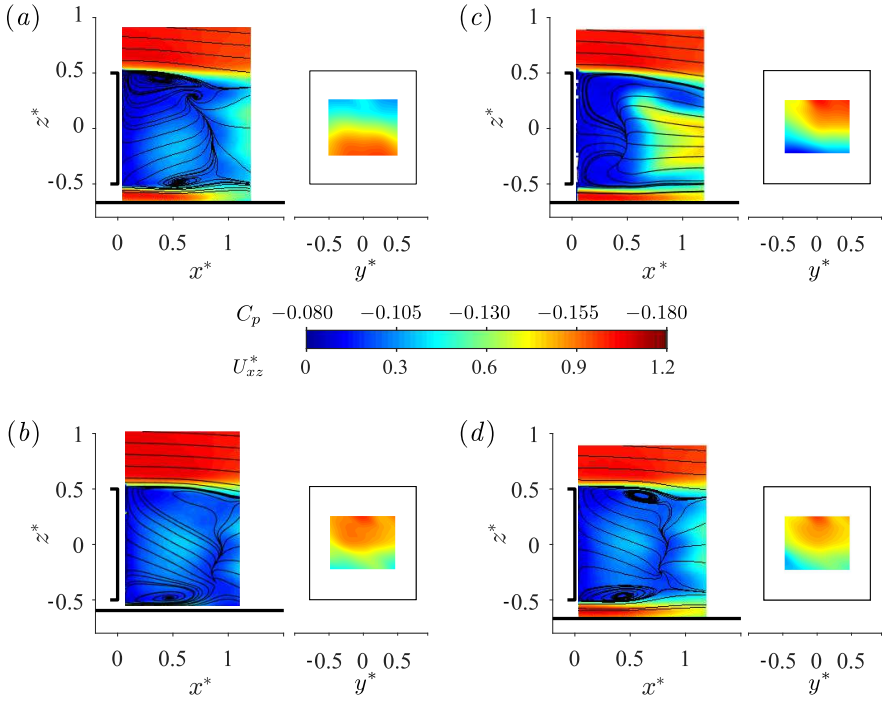

FIGURE 19. Cross-sections of the mean velocity field for the boat-tailed body visualized using streamlines superimposed to the modulus of the components in the vertical plane (x^*, z^*) for (a) baseline configuration ($\alpha = \beta = 0^\circ$, $c^* = 0.168$), (b) $\alpha = \beta = 0^\circ$, $c^* = 0.060$, (c) $\alpha = 0^\circ$, $\beta = -5^\circ$, $c^* = 0.168$, (d) nose-down configuration $\alpha = -0.6^\circ$ ($\beta = 0^\circ$). The associated mean base pressure distributions $C_p(y^*, z^*)$ are also provided.

3.2.2. *Exploration of the most probable states*

We now investigate the wake reversals with yaw for different fixed ground clearances: $c^* = 0.060$; 0.080; 0.124; 0.168 and a pitch angle set at $\alpha = 0^\circ$. With no yaw angle, we can see from figure $15(a, b)$ that these ground clearances successively correspond to a locked positive vertical gradient for $c^* = 0.060$, a bi-stable dynamics for $c^* = 0.080$ and a locked negative vertical gradient for $c^* = 0.124$ and $c^* = 0.168$. It is remarkable that the ground clearance has almost no effect on the gradient modulus in figure $15(c)$. So, it seems that the ground orientates the unstable wake with a positive vertical gradient for small c^* and with a negative vertical gradient for large c^*. At large ground clearance we would have expected the ground to become irrelevant and that the recovery of the top/down symmetry of the flow would have led to a bi-stable dynamics independently of the ground proximity. It is then the presence of the four supports that is responsible for the locked wake orientation at large ground clearance.

Sensitivity analyses with the yaw angle limited to $\beta \in [-6^\circ, 0^\circ]$ are presented in figure 20. For clarity, we extract the branches of most probable gradients using the following technique. The location of the maxima of each branch of the sensitivity maps such as the one given in figure 16 for $c^* = 0.168$ are identified for each yaw angle. Due to the normalization, the first maximum is 1, and a second maximum is plotted only if its value is larger than 0.10. This means that the second state is considered only if its probability exceeds approximately 10% of the observation time. The corresponding states for the vertical gradient component g_z^* are shown in figure $20(a)$. They form two distinctive branches, branch P for positive gradients, and branch N for negative

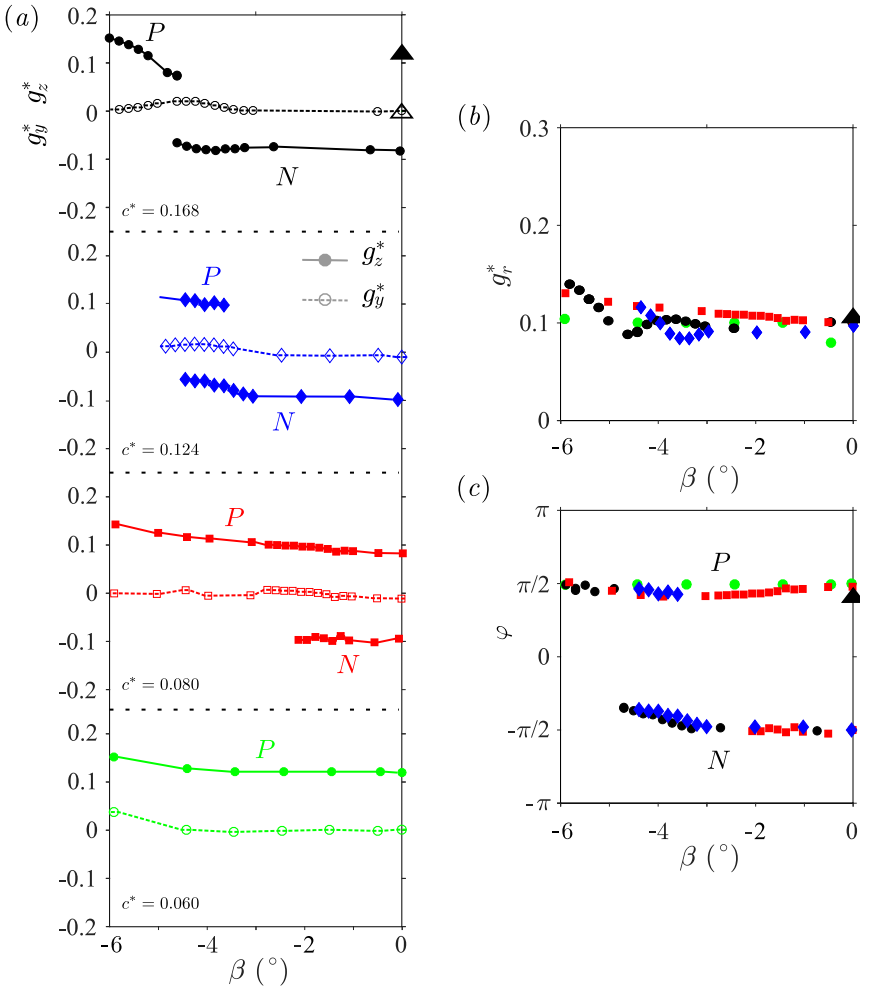

FIGURE 20. Most probable pressure gradients for the boat-tailed body g_y^* and g_z^* (a), g_r^* (b) and φ (c) versus the yaw angle at different ground clearances (with descending values from top to bottom in a). The triangles at $\beta = 0°$ correspond to the experiment with a fifth cylindrical support (see text).

gradients. Besides, the most probable horizontal component g_y^* of the gradient remains close to zero with little evolution for yaw around the switch for the two largest ground clearances. Except for the smallest ground clearance $c^* = 0.060$, large yaw angles select the P state. The larger the ground clearance, the larger the yaw angle at which the P state is selected.

In order to evidence the important role of the four supporting cylinders in the state selection mechanism, a fifth identical support is placed between the two front cylinders for $c^* = 0.168$. This experimental point is indicated by the black triangle in figure 20 that clearly shows a permanent wake reversal from branch N to branch P. On the basis of this simple experiment, one can draw a plausible mechanism for the change of branch as yaw increases. It is likely that in yaw conditions, the wake of the front leeward support that develops under the body gets closer to the mid-track of the base as the yaw increases, resulting in the wake reversal.

For yaw angles $|\beta| < 3°$, and independently of the ground clearance, the modulus

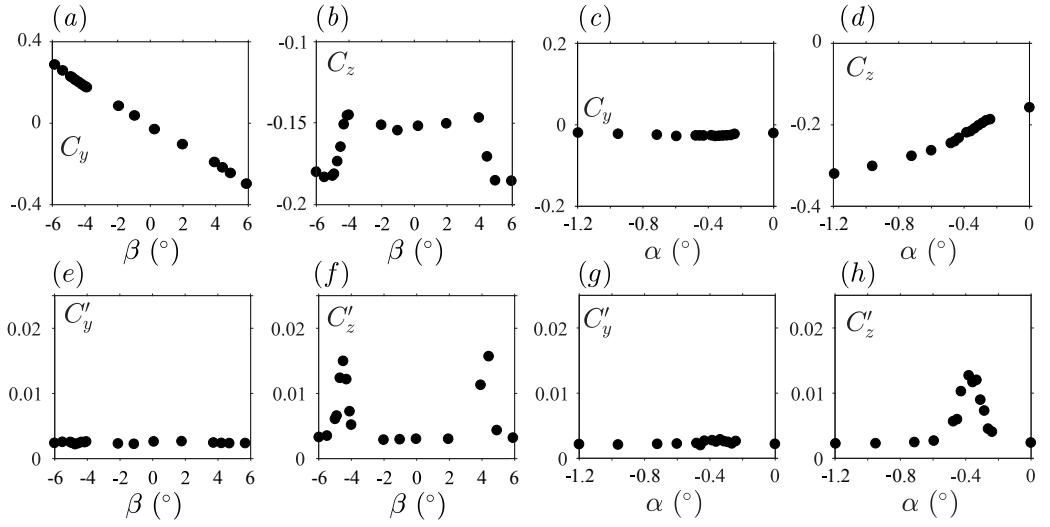

FIGURE 21. Mean (top row) and fluctuating (bottom row) cross-flow force coefficients vs. yaw (a, b, e, f) and pitch angle (c, d, g, h) for the boat-tailed body.

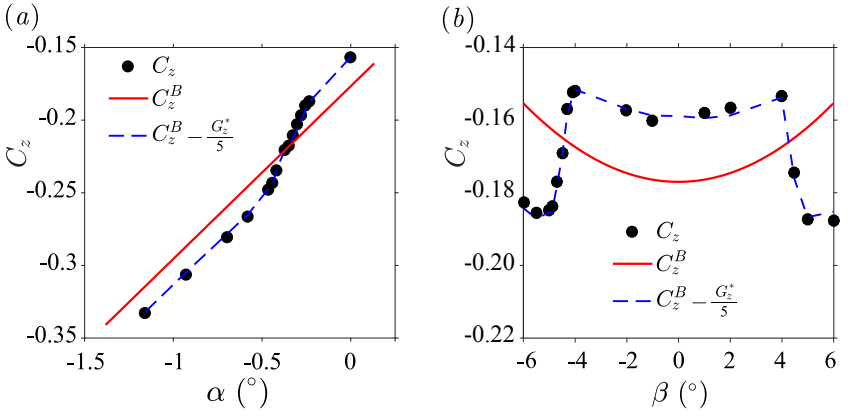

FIGURE 22. Mean lift coefficient vs. inclination of the boat-tailed body. The measured force coefficient (symbols) are compared to the *basic flow* coefficient (red line) and coefficient computed from equations (3.7a) (blue dashed line, see text). (a) Pitch angle sensitivity, (b) yaw angle sensitivity.

shown in figure 20(b) is found to be almost constant and the gradient has only two opposite phase orientations $+\pi/2$ for branch P and $-\pi/2$ for branch N, as can be seen in figure 20(c). For larger yaw $|\beta| > 3°$ the N state becomes yaw dependent and the modulus not as well defined.

3.2.3. *Global force sensitivity versus wake aerodynamic loading*

The y- and z-components of the mean force coefficients obtained for small yaw and pitch inclinations around the baseline are shown in figure 21$(a-d)$. With respect to the yaw angle β, C_y in figure 21(a) has a linear evolution showing that it is not influenced by the z-instability. Accordingly, the fluctuations (figure 21e) are small independently of the angle. On the contrary, the behavior of the mean lift coefficient C_z (figure 21b) is strongly impacted by the selected wake state which reveals two distinctive levels corresponding each to one wake orientation, either at $C_z \simeq -0.14$ for the P state or at $C_z \simeq -0.18$ for

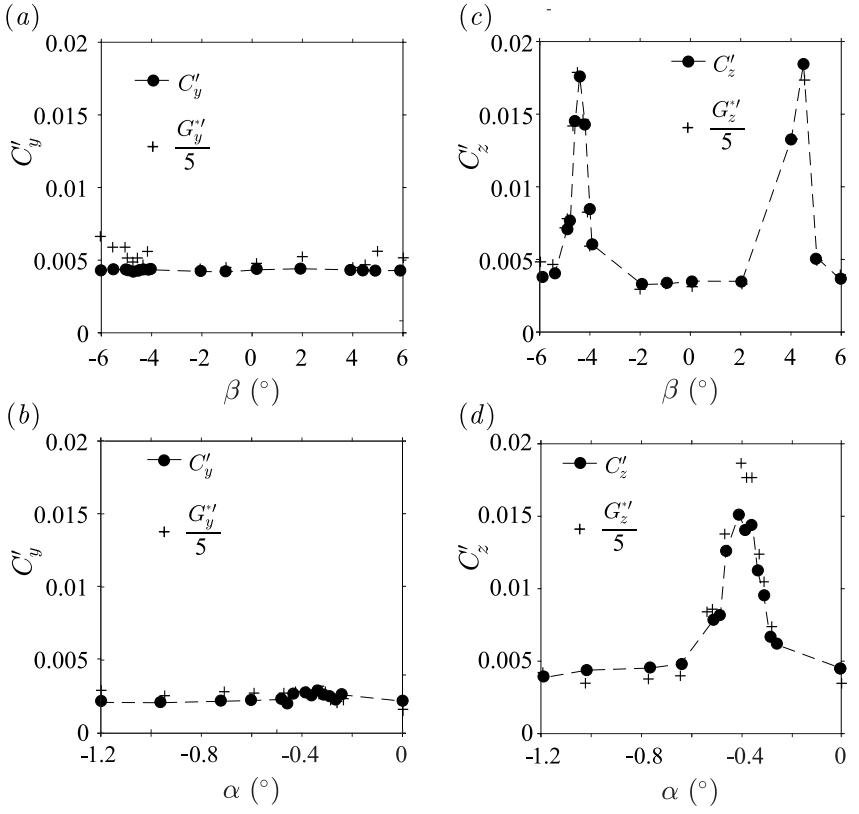

FIGURE 23. Components of the fluctuating force coefficients C'_y and C'_z (filled circles) compared to the fluctuation base pressure gradient $G^{*\prime}_y$ and $G^{*\prime}_z$ (crosses) vs. yaw β (top row) and pitch angle α (bottom row) for the boat-tailed geometry.

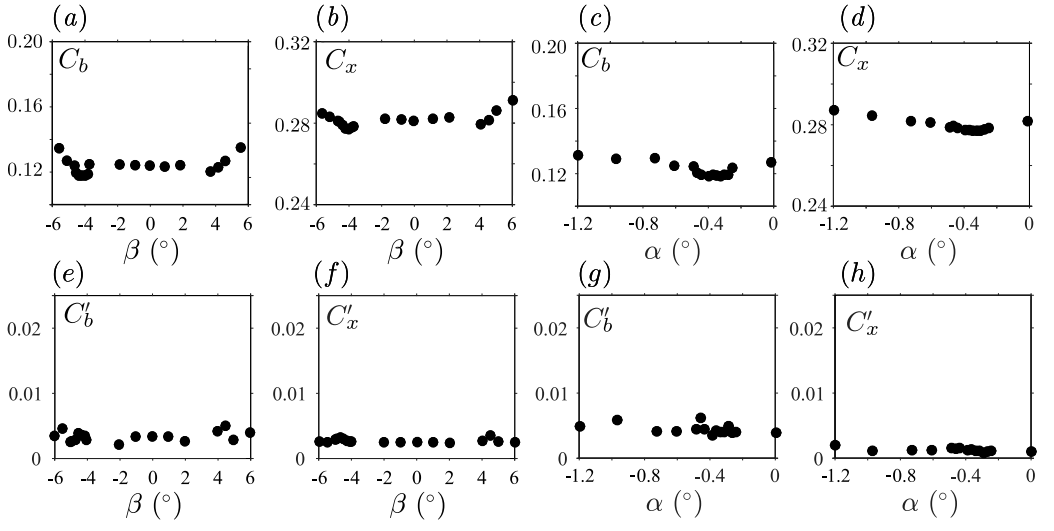

FIGURE 24. Mean (top row) and fluctuating (bottom row) drag force and base suction coefficients vs. yaw (a, b, e, f) and pitch angle (c, d, g, h) for the boat-tailed geometry.

the N state. As expected, there is a fluctuation crisis during the bi-stable dynamics at the transitions around $\pm 4^\circ$ as shown in figure 21(f).

For the pitch experiments with varying α, neither C_y in figure 21(c) nor its fluctuation C_y' in figure 21(g) are influenced by the z-instability. In contrast, the mean lift coefficient C_z in figure 21(d) and its fluctuation C_z' in figure 21(h) reveal the z-instability. The transition between the two states is clearly observable in both figures around $\alpha \simeq -0.4^\circ$. Actually the transition in pitch of the z-instability is similar to that in yaw of the y-instability when compared to figures 11(a, e).

We now look for a relationship between the mean gradient G_z^* and C_z as we did in figure 12(a) between G_y^* and C_y for the y-instability. For pitch sensitivity, C_z measurements reported in figure 22(a) suggest that the mean lift coefficient C_z^B obtained without the instability would be a linear function of the pitch angle α. The *basic flow* coefficient $C_z^B = 0.11\alpha - 0.177$ (where α is expressed in degrees) is shown in figure 22(a) as the red straight line. We recall that the superscript ^{B} refers to as the *basic flow* that is the flow without the instability as introduced in § 3.1.3. For the yaw sensitivity experiment, C_z measurements reported in figure 22(b) have a quadratic dependency that is not present in g_z^* shown in figure 16(b). Thus the quadratic dependency should be ascribed to the basic flow. The basic flow coefficient $C_z^B(\beta) = 6 \times 10^{-4}\beta^2 - 0.177$ (where β is expressed in degrees) is shown as the red curve in figure 22(b). For both pitch and yaw sensitivities, the blue dashed lines in figure 22 combines the base pressure gradient and the lift of the basic flow and shows satisfactorily a relationship:

$$C_z = C_z^B - \frac{G_z^*}{5} \tag{3.5}$$

The strength of the z-instability contribution to the lift coefficient, given by $C_z - C_z^B$ for either a pure P state or N state of the wake, is found to be approximately 0.02 as for the y-instability. Since the side force coefficient C_y is not affected by the instability, one should have

$$C_y = C_y^B \tag{3.6}$$

Both mean relationships (3.5) and (3.6) suggest the instantaneous expressions:

$$c_z(t^*) = C_z^B - \frac{g_z^*(t^*)}{5} \tag{3.7a}$$

$$c_y(t^*) = C_y^B - \frac{g_y^{*\prime}(t^*)}{5} \tag{3.7b}$$

Figure 23 shows the measured force fluctuation compared to the fluctuation computed from (3.7) using the base pressure gradient. These reasonably good agreements lead to similar relationships as (3.2) and (3.4) obtained for the y-instability, but with an exchange between the y- and the z-directions.

As displayed in figures 24($a - d$), the wake dynamics associated with the z-instability has almost no influence on either the drag or the base suction. The fluctuations remain one order of magnitude smaller than those of the lateral force coefficients (observed around 0.02 in figure 23). An interesting result is that drag (or equivalently base suction) is found to be the smallest during the bi-stable dynamics, either around $\beta = \pm 4.5^\circ$ for the yaw experiment or around $\alpha = \pm 0.4^\circ$ for the pitch experiment. This can be explained by the low-drag events related to wake switching as reported in Evrard *et al.* (2016).

Geometry	$(c^*, \alpha, \beta)_{switch}$	Δc^*	$\Delta\alpha$	$\Delta\beta$
Square-back	$(0.168, 0°, 0°)$	...	$1.5°$	$1°$
Boat-tailed	$(0.080, 0°, 0°)$	0.02	...	$5°$
”	$(0.124, 0°, \pm 4.0°)$	...	...	$1°$
”	$(0.168, 0°, \pm 4.5°)$	...	...	$0.2°$
”	$(0.168, -0.4°, 0°)$	...	$0.2°$	...

TABLE 3. Recap of the switch parameters $(c^*, \alpha, \beta)_{switch}$ at which state P and state N have same probability for the Ahmed bodies presented in §§ 3.1, 3.2. Δ denotes the range of variation of x (while the two other parameters are kept at the switch position) $x \pm \Delta x/2$ of bi-stable dynamics. Outside this range, a wake state either P or N is permanently selected.

4. Discussion

The experimental analysis provides conditions for which the wake is highly sensitive to the body orientation and ground clearance. These conditions are met each time variations are considered around the switch between the two branch solutions P and N. Table 3 recapitulates these positions for both flat-backed Ahmed bodies, and gives the sensitivity range of each parameter of the studies. In the following discussions, we try to clarify the key role played by the phase dynamics of the unstable wake and, based on our experimental results, propose a mechanism of phase dynamics adaptation to the body inclination, the ground proximity and the presence of the body supports.

4.1. *On the role of the phase dynamics of the unstable wake*

In the saturated regime of the instability ($c^* > c^*_S$), the investigation of the base pressure gradient in polar form (g^*_r, φ) indicates a permanent large modulus. For the square-back after body, it is within the range $0.15 < g^*_r < 0.2$ independently of the explored pitch and yaw misalignments of the body, while using the cavity, it drops to values below 0.1. The stabilization due to the cavity confirms that the large modulus results from the natural instantaneous asymmetry associated with the instability of the wake. Such asymmetry can be observed in the z-direction in many recent publications about rectangular-based bodies (Barros *et al.* 2016; McArthur *et al.* 2016; Castelain *et al.* 2018; Schmidt *et al.* 2018).

Due to the shape of the base, the modulus is larger when the gradient is horizontal $g^*_r(0 \text{ or } \pi) \simeq 0.187$ than vertical with $g^*_r(\frac{\pi}{2}) \simeq 0.159$. A similar observation is reported in Barros *et al.* (2017) where different gradient orientations were obtained by disturbing the flow in the ground clearance with small bodies of varying sizes. Since the ratio between the two orientations is very close to the rectangular base ratio W^*, we can propose a simple interpretation based on geometrical arguments. The idea is to introduce the non-axisymmetry of the after body using different characteristic length-scales in g_y and g_z directions. We then simply do the transformation:

$$\begin{aligned} g_y &= W^* g_y^{\mathcal{A}} \\ g_z &= g_z^{\mathcal{A}} \end{aligned} \tag{4.1}$$

where superscript $\mathcal{A}$ stands for the axisymmetric wake having a constant modulus $g_r^{\mathcal{A}}$ independently to its orientation. Making use of the transformation (4.1):

$$\hat{g}^{\mathcal{A}} = \frac{g_y}{W^*} + \mathrm{i} g_z$$

and

$$(g_r^{\mathcal{A}})^2 = g_r(\varphi)^2 \left(\frac{\cos^2 \varphi}{{W^*}^2} + \sin^2 \varphi \right)$$

Noting that $g_r\left(\frac{\pi}{2}\right) = g_r^{\mathcal{A}}$, we obtain for the dimensionless modulus of the non-axisymmetric wake:

$$g_r^*(\varphi) = \frac{g_r^*\left(\frac{\pi}{2}\right)}{\sqrt{\left[1 - \left(1 - \frac{1}{{W^*}^2}\right)\cos^2 \varphi\right]}} \tag{4.2}$$

The ratio of the horizontal to the vertical component of the base gradient is given by $g_r^*(0)/g_r^*\left(\frac{\pi}{2}\right) = W^*$. This relation is in good agreement with the measurements in figure 5(c), where the white symbols are the time average $\overline{g_r^*}$ of the formula (4.2) computed from the time series $\varphi(t)$ and with $g_r^*(\frac{\pi}{2}) = 0.159$.

The simple model (4.2) describes an elliptical modulation of the gradient modulus with its orientation. It is likely that the right angles of the rectangular base do not introduce any singularities in the base pressure gradient modulus. Similarly we computed both components as ($\overline{g_y^*} = \overline{g_r^* \cos\varphi}|_{\varphi>\pi/2}$, $\overline{g_y^*} = \overline{g_r^* \cos\varphi}|_{\varphi<\pi/2}$) shown in figure 5($a$) and $g_z^* = \overline{g_r^* \sin\varphi}$ shown figure 5(b) with white symbols. It is successively repeated in figure 3 and figure 4 for the two other sensitivity experiments. Hence, the good agreements with the sensitivity maps indicate that regardless of the body inclination and ground clearance above the critical value, the unstable wake obeys the modulus model (4.2). For the boat-tailed after body, mainly two opposite vertical orientations of the base pressure gradient are observed, $\varphi \simeq \pm\pi/2$ as can be seen in figures 15(d), 16(d) and 17(d). The corresponding modulus shown in figures 15(c), 16(c), 17(c) and recap in figure 20(b) remain almost constant $g_r^*(\frac{\pi}{2}) \simeq 0.1$ for yaw angles $|\beta| < 4°$ which is also consistent with the model. The smaller value of the gradient modulus compared to those of the square-back body is likely to be due to the different after body geometries that are not self-similar.

The observation that the base pressure gradient modulus of the unstable wake is mainly imposed by the base shape offers a simplification for the wake modelling. The key ingredient is actually the comprehension of the phase dynamics of a unique symmetry-breaking mode of a known intensity given in (4.2) since the base gradient of the turbulent wake may be written as:

$$g_y^*(t) = g_r^*(\varphi)\cos\varphi, \quad g_z^*(t) = g_r^*(\varphi)\sin\varphi, \tag{4.3}$$

We have seen that the axisymmetric turbulent wake model of Rigas *et al.* (2014, 2015) produces radial statistics in agreement with the pressure gradient modulus statistics in figures 6 and 18. It may then be modified in future work to consider the asymmetry of the body base. However, the real challenge is to take into account of the asymmetry in the phase dynamics modelling by introducing a specific potential. A fundamental question is how the phase dynamics adapts to the non-axisymmetric environment of the wake flow introduced by the rectangular base, the body inclination, ground proximity and body supports. In the following, we discuss how such symmetrical defects constrain the phase dynamics of the unstable wake.

4.2. *Phase dynamics adaptation and consequences for cross flow force*

A remarkable result is that large discontinuous transitions of all sensitivity experiments are always observed in the horizontal component g_y^* (respectively, vertical component g_z^*) of the base pressure gradient for the square-back (respectively boat-tailed) body.

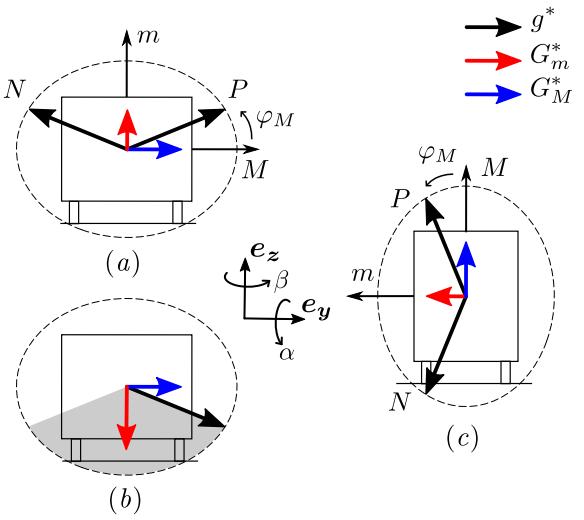

FIGURE 25. Phase dynamics adaptation of the base pressure gradient of the unstable wake for the y-instability (a, b) and z-instability (c). The modulus of the pressure gradient is depicted by the dashed ellipse following (4.2). The (red) mean minor-component G^*_m equals that of the basic flow (4.5), thus restricting the possible phase dynamics. It is a bi-stable distribution with the two possible orientations P and N in (a) for nose-down pitch and in (c), and a continuous distribution in the grey area in (b) for nose-up configuration. The (blue) mean major component G^*_M depends on the states probability distribution given by κ following (4.6).

These two observations justify the terminologies *y-instability* and *z-instability* used in the paper. The component of the gradient that undergoes these discontinuities between opposite values is then always the one aligned with the major axis of the rectangular base, since the base aspect ratio is larger than 1 for the square-back body and smaller than 1 for the boat-tailed body. In contrast, the component in the minor axis direction of the base (g^*_z for the y-instability, and g^*_y for the z-instability) present continuous evolution with ground clearance, yaw and pitch.

New definitions are necessary to set a common framework for both the y-instability and z-instability. For the remainder of the paper, m subscript will denote the minor component and M subscript the major component of the rectangular base axes system as displayed in figure 25. We also define the phase orientation φ_M computed from the major axis. In this coordinate system, the base gradient (4.3) becomes:

$$g^*_M(t) = g^*_r(\varphi_M)\cos\varphi_M, \quad g^*_m(t) = g^*_r(\varphi_M)\sin\varphi_M \tag{4.4}$$

In addition, the aspect ratio in $g^*_r(\varphi_M)$ defined by (4.2) should be re-defined as $W^* = \frac{l_M}{l_m} > 1$, where l_M is the largest side of the rectangular base and l_m the smallest.

For the square-back body, both the mean of this minor gradient component $G^*_m = G^*_z$ and minor force coefficient component $C_m = C_z$ deserve specific attention when compared to the case with a rear cavity. In figure 11(d), the rear cavity has no effect on the mean lift component while the instability is suppressed. The asymmetry of the mean velocity in the vertical plane is also very similar without (figure 7a, c, e) and with (figure 10a, c, e) the cavity. The main difference being the larger bubble length associated with higher base pressure for the rear cavity (Evrard *et al.* 2016). Hence, the observed vertical asymmetries introduced by the pitch are not resulting from the wake instability but from the inclination of the body. It then appears that the minor component of the base pressure gradient G^*_m matches in average the component that would have been obtained without

the instability ${G_m^*}^B$, *i.e.* that of the so-called *basic flow* as introduced in section § 3.1.3:

$$G_m^* = \overline{g_r^*(\varphi_M)\sin\varphi_M} = {G_m^*}^B \tag{4.5}$$

Assuming that there are only two observable mirror states for the wake, then the gradient orientation will take two values, φ_M for state P and $\pi - \varphi_M$ for state N with respective probability denoted by κ and $1-\kappa$. The mean matched minor component (4.5) simply becomes ${G_m^*}^B = G_m^* = g_r^*(\varphi_M)\sin\varphi_M$ which, with (4.2) fully determines φ_M and hence the two possible wake orientations as depicted in figures 25(a, c). Consequently, the mean major component is:

$$G_M^* = g_r^*(\varphi_M)(2\kappa - 1)\cos\varphi_M \tag{4.6}$$

with fluctuation ${G_M^*}' = 2\sqrt{\kappa(1-\kappa)}g_r^*(\varphi_M)\cos\varphi_M$. There are two distinctive cases to consider for wake orientation selections whether the minor axis corresponds to a reflectionnal symmetry or not.

For the y-instability (figure 25a), the minor axis is a reflectionnal symmetry axis when the ground clearance and pitch angle are varied. The symmetry implies equal exploration of both states, *i.e.* $\kappa = 1/2$. Because of unavoidable symmetry defects coming from different sources, equal exploration is not always observed for ground clearance (figure 3), and pitch angle (figure 5) variations. Making use of the adaptation mechanism (4.5), we can see for the ground clearance variation in figure 3, how both the ground and body supports produce the minor component in figure 3(b) on which the unstable wake adapts to provide the wake orientation φ_M in figure 3(d). Note that because of the body supports, large ground clearances never restore the reflectionnal symmetry with respect to the major axis (*i.e.* top/bottom symmetry), there is then no reason for the vertical gradient component to vanish at large ground clearances in figure 3(b). Similarly for the pitch variation in figure 5, the minor component that varies monotonically in figure 5(b) with the angle α imposes through relation (4.5) the two states orientations of the bi-stable dynamics φ_M and $\pi - \varphi_M$ that change continuously from $\varphi_M = +\pi/2$ to approximately 0. The same global orientation change of the unstable wake was observed in Barros *et al.* (2017) referred to as *symmetry exchange* by increasing the size of a small disturbing body placed between the ground and the Ahmed body. In the context of the adaptive mechanism, it is likely that the disturbing body modifies the minor component of the base pressure gradient. An interesting consequence of the adaptation condition is that bistability occurs only if the intensity of the minor component is smaller than the modulus $g_r^*(\varphi_M)$. When they are both equal, the unstable wake orientation becomes aligned with the minor component. This effect is clearly seen for the pitch sensitivity with y-instability in figure 5(b) when $\alpha \simeq -1°$. It seems that the gradient modulus saturates to that of the unstable wake even for larger pitch. For nose-up configurations with pitch angles $\alpha > 0.5°$ the bi-stable dynamics turns into a random wake rotation similar to the dynamics described in Rigas *et al.* (2014, 2015) but whose phase dynamics still fulfills the condition (4.5) as depicted by the schematic drawing in figure 25(b).

In the second case for which the minor axis is not a reflectionnal symmetry, $\kappa \neq 1/2$. The probability κ can either remain in the range $]0, 1[$ for small reflectionnal symmetry breaking as in yaw experiment for the y-instability with $|\beta| < 0.5°$ (figure 4) or more simply be $\kappa = 1$ or 0, respectively associated with permanent state P or state N lock-in. These lock-ins, related to a lack of symmetry, are observed with the z-instability for all explored ground clearances (figure 15), yaw (figure 16) and pitch angles (figure 17). In each of these sensitivity maps, a discontinuous transition accompanied by a bi-stable behavior between the two states is observed. It is likely that a *symmetry compensation* occurs to satisfy equal exploration of the two states by restoring an effective $\kappa = 1/2$.

Although this might imply several geometrical defects, we attempt in the following to give the main ones. For bistability obtained at $c^* = 0.080$ in figure 15, we believe that the ground proximity and the supports are involved. For the two other bi-stable dynamics observed at larger ground clearance in figures 16 and 17, we believe that the ground proximity plays a minor role compared to those of the supports and the body inclination. In figure 17, the supports and the pitch inclination should compensate. For the bistability observed in figure 16, the change of the support configurations in yaw introduces the compensation due the wake of the front leeward support. As an attempt to summarize the origin of the observed wake locks-in, our results suggest that supports are favourable to state N when the body has no yaw, to state P with yaw, that ground proximity is favourable to state P and pitch down to state P. Figure 20(a) gives a consistent overview of the state selection in yaw angle and ground clearance variations.

The adaptation of the mean *minor* component of the base pressure gradient to that of the *basic flow* (assumed to be steady) suggests the following expressions for the instantaneous base pressure gradient of the unstable wake :

$$g^*_m(t) = {G^*_m}^B + g'_m(t) \tag{4.7a}$$

$$g^*_M(t) = G^*_M + g'_M(t) \tag{4.7b}$$

These relations can be used to estimate the cross flow force coefficients for which we assume two contributions. A first one results from the flow without the instability: the *basic flow*. The *basic flow* force coefficients have a continuous evolution with inclination and ground clearance. The second contribution accounts for the unstable wake:

$$c_m(t) = {C_m}^B + A{g^*}'_m(t) \tag{4.8a}$$

$$c_M(t) = {C_M}^B + Ag^*_M(t) \tag{4.8b}$$

Notice that because of the unstable wake adaptation (4.5), the mean minor gradient is absent in (4.8a) since it equals those of the *basic flow* and then taken into account in ${C_m}^B$. These two relations are the ones found experimentally in (3.2) and (3.4) for the y-instability and (3.7) for the z-instability confirming that the adaptation mechanism is consistent with all lateral force measurements. The coefficient A is found to be 1/10 for the square-back body and 1/5 for the boat-tailed after body. We attribute the discrepancy to the difference in the geometries. However, the contribution of the wake instability to the side force coefficients is given by $A|G^*_M(\varphi_M = 0, \pi)| \simeq 0.02$ for both after bodies where $M = y$ for the square-back after body subjected to the y-instability and $M = z$ for the boat-tailed after body subjected to the z-instability. It is a substantial contribution to the total aerodynamics loading of the bodies since it represents approximately 7% of the drag coefficient and approximately 12% to 16% (depending on the geometry) of the lift coefficient of the baselines.

5. Conclusion

The unstable turbulent wake of two flat-backed Ahmed bodies with different rectangular base aspect ratio have been investigated varying three geometrical parameters: ground clearance, pitch and yaw angles. The experimental results are presented as sensitivity analyses of the modulus and phase of the base pressure gradient to these geometrical parameters. For any ground clearance above a critical value of $c^*_S \simeq 0.1$ and for any pitch or yaw angles explored, the large modulus indicates the permanent presence of the static symmetry-breaking instability reported in Grandemange *et al.* (2012).

The strength of the instability is larger when the wake is orientated along the major

axis of the vertical base rather than along its minor axis in a proportion equal to the base ratio. A simple model that only depends on the vertical base shape is provided for the base gradient. The model gives an elliptical modulation of its modulus with its orientation. The global property of the unstable wake then simplifies into a single mode defined from this modulus and a phase orientation that is the key ingredient of the dynamics.

When changing the body inclination or ground clearance, it is found that the minor component of the base pressure gradient always matches that of the flow with no instability which, for a given modulus, constrains the possible phase dynamics. For most cases, two possible phase orientations are found corresponding to the two flow states belonging to the branch solutions P or N.

The probability of each flow state is sensitive to the geometrical environment of the wake such as the ground proximity, the body supports and the body inclination. Bi-stable dynamics are observed during transitions in which the probability of each flow state is equal. This happens in symmetrical configurations as for the y-instability or in asymmetrical configurations as for the z-instability. The latter case involves compensation effects between two different origins of the asymmetry. An experimental derivation of the cross flow force from the base pressure gradient dynamics has been proposed emphasizing the major impact of the unstable wake dynamics.

Eventually, a natural perspective to this work is the application to industrial car aerodynamics. A transition in yaw similar to that observed for the body subjected to the z-instability (§ 3.2.2) has been reported for a Renault Kangoo by Cadot *et al.* (2016) and Bonnavion *et al.* (2017). Similar analyses as those presented in this paper will be investigated for real cars to confirm the presence of the static symmetry-breaking instability in the wakes.

Acknowledgment

The authors would like to thank Édouard Boujo for his critical reading of the manuscript and to acknowledge the CNRT R2A (*Centre National de Recherche Technologique en Aérodynamique et Aéroacoustique des Véhicules Terrestres*, National center for technological research in aerodynamics and aeroacoustics of ground vehicles) for funding this work. The authors are also thankful to Vincent Herbert (Groupe PSA), Sylvain Parpais (Groupe Renault), Rémi Vigneron (GIE-S2A) and Jean Délery as well as the staff of the GIE-S2A among whose Philippe Thébault, David Pérez and Éric Van Grevenynghe for their support and help during the tests and for PIV post-processing. The ground clearance and pitch adjustment system of the Ahmed body was designed, manufactured and installed by Lahcène Cherfa who is gratefully acknowledged.

Supplementary movie

A supplementary movie is available (Movie).

Caption: Instantaneous base pressure distribution $c_p(y^*, z^*, t^*)$ for nose-down, baseline and nose-up configurations corresponding to the time series in figure 6. The signals are low-pass filtered by an averaging on a sliding window of time duration $t^*_w = 33.3$.

REFERENCES

Ahmed, S.R., Ramm, G. & Faitin, G. 1984 Some salient features of the time-averaged ground vehicle wake. *SAE Technical Paper Series* **840300**.

Barros, D., Borée, J., Cadot, O., Spohn, A. & Noack, B. 2017 Forcing symmetry exchanges and flow reversals in turbulent wakes. *J. Fluid Mech.* **829** (1), R1.

Barros, D., Borée, J., Noack, B. R., Spohn, A. & Ruiz, T. 2016 Bluff body drag manipulation using pulsed jets and Coanda effect. *J. Fluid Mech.* **805**, 422–459.

Barros, D., Ruiz, T., Borée, J. & Noack, B.R. 2014 Control of three-dimensionnal blunt body wake using low and high frequency pulsed jets. *Intl J. Flow Control* **6** (1), 61–74.

Bonnavion, G., Cadot, O., Évrard, A., Herbert, V., Parpais, S., Vigneron, R. & Délery, J. 2017 On multistabilities of real car's wake. *J. Wind Eng. Ind. Aerodynamics* **164**, 22–33.

Brackston, R. D., García De La Cruz, J.M., Wynn, A., Rigas, G. & Morrison, J. F. 2016 Stochastic modelling and feedback control of bistability in a turbulent bluff body wake. *J. Fluid Mech.* **802**, 726–749.

Cadot, O. 2016 Stochastic fluid structure interaction of three-dimensional plates facing a uniform flow. *J. Fluid Mech.* **794**, R1.

Cadot, O., Courbois, A., Ricot, D., Ruiz, T., Harambat, F., Herbert, V., Vigneron, R. & Délery, J. 2016 Characterisations of force and pressure fluctuations of real vehicles. *Int. J. Engineering Systems Modelling and Simulation* **8** (2), 99–105.

Cadot, O., Evrard, A. & Pastur, L. 2015 Imperfect supercritical bifurcation in a three-dimensional turbulent wake. *Phys. Rev. E* **91** (6), 063005.

Castelain, T., Michard, M., Szmigiel, M., Chacaton, D. & Juvé, D. 2018 Identification of flow classes in the wake of a simplified truck model depending on the underbody velocity. *J. Wind Eng. Ind. Aerodynamics* **175**, 352–363.

Evrard, A., Cadot, O., Herbert, V., Ricot, D., Vigneron, R. & Délery, J. 2016 Fluid force and symmetry breaking modes of a 3D bluff body with a base cavity. *J. Fluids Struct.* **61**, 99–114.

Evstafyeva, O., Morgans, A. S. & Dalla-Longa, L. 2017 Simulation and feedback control of the Ahmed body flow exhibiting symmetry breaking behaviour. *J. Fluid Mech.* **817**, R2.

Gentile, V., Schrijer, F.F.J., Van Oudheusden, B.W. & Scarano, F. 2016 Low-frequency behavior of the turbulent axisymmetric near-wake. *Physics of Fluids* **28** (6), 065102.

Gentile, V., Van Oudheusden, B.W., Schrijer, F.F.J. & Scarano, F. 2017 The effect of angular misalignment on low-frequency axisymmetric wake instability. *J. Fluid Mech.* **813**, R3.

Grandemange, M., Gohlke, M. & Cadot, O. 2012 Reflectional symmetry breaking of the separated flow over three-dimensional bluff bodies. *Phys. Rev. E* **86**, 035302.

Grandemange, M., Gohlke, M. & Cadot, O. 2013*a* Bi-stability in the turbulent wake past parallelepiped bodies with various aspect ratios and wall effects. *Phys. Fluids* **25**, 095103.

Grandemange, M., Gohlke, M. & Cadot, O. 2013*b* Turbulent wake past a three-dimensional blunt body. Part 1. Global modes and bi-stability. *J. Fluid Mech.* **722**, 51–84.

Grandemange, M., Gohlke, M. & Cadot, O. 2014*a* Statistical axisymmetry of the turbulent sphere wake. *Exp. Fluids* **55** (11), 1–10.

Grandemange, M., Gohlke, M. & Cadot, O. 2014*b* Turbulent wake past a three-dimensional blunt body. Part 2. Experimental sensitivity analysis. *J. Fluid Mech.* **752**, 439–461.

Hucho, W.H. 1998 *Aerodynamics of road vehicles*. SAE International.

Li, R., Barros, D., Borée, J., Cadot, O., Noack, B. R. & Cordier, L. 2016 Feedback control of bimodal wake dynamics. *Exp. Fluids* **57** (10), 158.

Lucas, J.-M., Cadot, O., Herbert, V., Parpais, S. & Délery, J. 2017 A numerical investigation of the asymmetric wake mode of a squareback Ahmed body – effect of a base cavity. *J. Fluid Mech.* **831** (1), 675 – 697.

McArthur, D., Burton, D., Thompson, M. & Sheridan, J. 2016 On the near wake of a simplified heavy vehicle. *J. Fluids Struct.* **66**, 293 – 314.

Pasquetti, R. & Peres, N. 2015 A penalty model of synthetic micro-jet actuator with application to the control of wake flows. *Comput. Fluids* **114** (0), 203–217.

Pavia, G. & Passmore, M. 2018 Characterisation of Wake Bi-stability for a Square-Back Geometry with Rotating Wheels. In *Progress in Vehicle Aerodynamics and Thermal Management* (ed. J. Wiedemann), pp. 93–109. Springer International Publishing.

Pavia, G., Passmore, M. & Sardu, C. 2018 Evolution of the bi-stable wake of a square-back automotive shape. *Exp. Fluids* **59** (1), 20.

Perry, A., Almond, M., Passmore, M. & Littlewood, R. 2016*a* The study of a bi-stable wake region of a generic squareback vehicle using tomographic PIV. *SAE Int. J. Passeng. Cars - Mech. Syst* **9**, 2.

Perry, A., Pavia, G. & Passmore, M. 2016*b* Influence of short rear end tapers on the wake of a simplified square-back vehicle: wake topology and rear drag. *Exp. Fluids* **57** (11), 169.

Pier, B. 2008 Local and global instabilities in the wake of a sphere. *J. Fluid Mech.* **603**, 39–61.

Rigas, G., Morgans, A.S., Brackston, R. D. & Morrison, J.F. 2015 Diffusive dynamics and stochastic models of turbulent axisymmetric wakes. *J. Fluid Mech.* **778**, R2.

Rigas, G., Oxlade, A.R., Morgans, A.S. & Morrison, J.F. 2014 Low-dimensional dynamics of a turbulent axisymmetric wake. *J. Fluid Mech.* **755**, R5.

Roshko, A. 1993 Perspectives on bluff body aerodynamics. *J. Wind Eng. Ind. Aerodynamics* **49** (1-3), 79–100.

Schmidt, H.-J., Woszidlo, R., Nayeri, C. N. & Paschereit, C. O. 2018 The effect of flow control on the wake dynamics of a rectangular bluff body in ground proximity. *Exp. Fluids* **59** (6), 107.

Vilaplana, G., Grandemange, M., Gohlke, M. & Cadot, O. 2013 Experimental sensitivity analysis of the global mode of a sphere turbulent wake using steady disturbances. *J. Fluids Struct.* **41**, 119–126.

Volpe, R., Devinant, P. & Kourta, A. 2015 Experimental characterization of the unsteady natural wake of the full-scale square back Ahmed body: flow bi-stability and spectral analysis. *Exp. Fluids* **56** (5), 22.